Synthesis, characterization, and thermodynamic study of selected Na-based zeolites

Bin Ma[a,*], Barbara Lothenbach[a,b]

[a] Laboratory for Concrete & Construction Chemistry, Swiss Federal Laboratories for Materials Science and Technology (Empa), 8600 Dübendorf, Switzerland

[b] Department of Structural Engineering, Norwegian University of Science and Technology (NTNU), 7491 Trondheim, Norway

[*] Corresponding author at: Laboratory for Concrete & Construction Chemistry, Swiss Federal Laboratories for Materials Science and Technology (Empa), 8600 Dübendorf, Switzerland.
E-mail address: bin.ma@empa.ch (B. Ma).

Abstract

Zeolites are crystalline aluminosilicates with three-dimensional framework structures that can form in alkali-activated cements, Roman cements, and the interaction zone of cements and clays. However, their stability domains are uncertain due to their high structural variability and the lack of experimental solubility data. Thermodynamic data were here determined for selected Na-based zeolites built from six different secondary building units that could possibly form in the interaction zones of cement/clay. The zeolites were synthesized by hydrothermal methods and full-scale characterized with respect to framework structures, extra-framework cations, Si/Al ratios, and water contents. Their thermodynamic properties were determined based on the experimental solubility products at different temperatures using GEMS. Predominance diagrams of zeolite-clay/mica-SiO_2/$Al(OH)_3$ minerals in the chemical sub-systems of Na_2O-SiO_2-Al_2O_3-H_2O were successfully established using PHREEQC-PhreePlot code. The experimentally derived thermodynamic data provide insights on the early stage of the zeolite ageing and predicting zeolite stability domains during cementitious material hydration.

Keywords

Zeolite; Solubility product; Thermodynamic data; Degraded cement/clay interface; Cemdata; Stability domain; Nuclear waste disposal.

1. Introduction

Zeolites have three-dimensional framework structures. Typically, their frameworks are negatively charged due to the partial (half in maximum) substitution of Si^{4+} by Al^{3+}, and the negative charge is balanced by exchangeable cations (e.g., Na^{+}, K^{+}, and Ca^{2+}) in the cages. The microporous structures and the exchangeable cations enable zeolites to have diverse applications in different areas, such as petrochemical industry, catalysis, agriculture, heat storage, and cement industry [1]. In cement industry, zeolites can be used as supplementary cementitious materials, which can reduce CO_2 emission by partially replacing cement clinkers [2]; the high content of alkalis generally present in zeolites accelerates the reaction of cement clinkers. Zeolites can also potentially form in alkali-activated cements [3, 4], have been observed in Roman cements [5] or possibly precipitate instead of expansive alkali silica reaction (ASR) products if sufficient aluminum is available [6].

Zeolites can also form as secondary mineral phases at the interaction zone of degraded cements and clays [7, 8], e.g. in underground concrete structures or cementitious nuclear waste repositories. Zeolitic precipitates, such as nitrate-sodalite, nitrate-cancrinite, and faujasite, could form from clays (e.g., illite, vermiculite, or montmorillonite) subjected to weathering in high-level radioactive tank waste leachate [9], such that cements, zeolites and clays can be expected to co-exist in long-term underground constructions [10, 11].

Although zeolites are used in diverse areas and are present in different cementitious systems, their stability and the conditions of formation or dissolution are still uncertain, as the compositions and structures of zeolites are quite variable and little experimental solubility data are available. The solubility products for different zeolites are typically determined from measured or calculated enthalpy and heat capacity data, which leads, due to the uncertainty associated with the measurements of enthalpy data, to significant errors on the solubility product. Due to the lack of experimental data, researchers tried developing "critical and systematic"

estimation strategies of thermodynamic data of zeolites [11, 12]. The standard Gibbs free energies of formation (ΔG_f^0) and standard enthalpies of formation (ΔH_f^0) has been calculated by the polymer model [13, 14], polyhedral model [15], exchange models [16], and phase relation methods [17]. The calculation of the standard entropy (S^0) and heat capacity (C_p^0) has been made typically using additivity methods [17-19]. However, unclear kinetics of mineralogical equilibrium/transformation and limited mineralogical and chemical compositions, makes this difficult and the resulting stability fields might not agree with experimental observation as discussed in Blanc et al. [11]. Problems arise with the completeness of the thermodynamic datasets, e.g., with $\Delta_f H^0$ and S^0 measured on minerals displaying slightly different compositions. Mineralogical determinations of zeolites are hard to be precise based on X-ray diffraction (XRD) alone. One way to verify the estimation models was to process solution experiments using well-defined zeolite structures. This underlines the need for systematic experimental determination of the solubility for different zeolites.

The internal consistency of thermodynamic data can be ensured considering the coexistence of cements, zeolites, and clays. Currently, the thermodynamic database of Cemdata'18 [20] mainly contains the data of cement phases but lacks the data for zeolites and clays. By complementing Cemdata'18 with the clay data from ThermoChimie [21] and determining the experimental data for zeolites (including Na-, K-, Ca-, and Mg-based forms), the global consistency in the framework of Cemdata'18 database could be verified in future. The objective of current study is to investigate the thermodynamic properties of Na-based zeolites that could possibly form in the cementitious system; data for zeolites containing Ca are discussed in [22]. High purity Na-based zeolites were synthesized by hydrothermal method and characterized. Their solubility products as a function of temperature were determined via dissolution experiments and further employed to generate the corresponding thermodynamic data (except for C_p^0) using GEMS. The currently generated data were compared with the relevant values in literatures. Thermodynamic modelling was conducted to predict the stable zeolite phases in a

degraded PC/rock system, and to verify the consistency between the newly generated data and the available databases as a function of Na^+/H^+ ratios and activities of $SiO_2(aq)$ and AlO_2^-. The experimentally derived thermodynamic data will allow us to predict zeolite stability domains in systems where zeolites could potentially exist.

2. Materials and methods

2.1. Materials

Sodium hydroxide pellets (NaOH, >99% purity, Emsure), potassium hydroxide pellets (KOH, >85% KOH basis, Sigma-Aldrich), and various aluminum and silica sources were used as the principal raw materials for the hydrothermal synthesis of zeolites. The aluminum sources used included sodium aluminate ($NaAlO_2$, technical grade, Sigma-Aldrich), aluminium hydroxide gel (50 wt.% Al_2O_3, Geloxal 10), and $Al_2(SO_4)_3 \cdot 18H_2O$ (chemical grade, Merck). Five kinds of silica sources were used, including aqueous colloidal silica (40 wt.% suspension in H_2O, Ludox HS-40 and AS-40), fumed silica (SiO_2, chemical grade, Aerosil 200), sodium metasilicate (Na_2SiO_3, reagent-grade, Aldrich), and sodium silicate solution (reagent-grade, Sigma-Aldrich). Where necessary in the synthesis, tetramethylammonium hydroxide pentahydrate (97% $(CH_3)_4N(OH) \cdot 5H_2O$, Sigma) and triethanolamine (98% $N(C_2H_4OH)_3$, Sigma-Aldrich) were introduced as structure-directing agents (SDAs). NaCl (≥99.5%, puriss p.a.) was bought from Sigma-Aldrich and used for cation exchange. Fresh Milli-Q water (18.2 MΩ·cm) was used for all solutions and suspensions.

Natural and commercial zeolites were collected for seeding during zeolite synthesis and for the determination of their thermodynamic properties. Scolecite (New Malden, U.K.) and mordenite (Alfa Aesar) were collected and used for seeding the synthesis of natrolite and mordenite, respectively. The commercial molecular sieve of zeolite 4Å purchased from Sigma-Aldrich was investigated as well in this study. All the natural and commercial zeolites were

crushed, picked, ground by an agate mortar, and passed through a 63-μm pore size stainless sieve.

2.2. Zeolite synthesis

Hydrothermal methods were used for the zeolite synthesis. Different alkali concentrations, Si/Al ratios, Al and Si sources, SDAs/seeds, and crystallization temperatures and durations were explored to obtain different types of pure zeolites (Table 1). Typically, the silica, aluminum and cation sources were mixed together in a highly basic medium. If needed, SDAs or seeds would be added as well in this mixing stage. The aqueous reaction mixtures were heated in temperature-controlled ovens from 80 to 200 ℃. Teflon vessels were used as reactors at crystallization temperatures below 110 ℃. When higher hydrothermal temperatures were required, Teflon-lined stainless steel autoclaves were employed. The hydrothermal synthesis of natrolite [23], low-silica gismondine P [24-26], and chabazite [27, 28], were modified based on the corresponding literature, while those of other zeolites were done according to Robson [29]. Regarding the selection of raw materials, priorities were given to commonly commercial chemicals, in order to facilitate successful synthesis repetitions by other researchers. The necessary modifications of recipes were explored, due to the different reactivity of the raw materials with those of the materials used in the literature. After crystallizing for different times (Table 1), the obtained solids were recovered by, in sequence, vacuum filtration, Milli-Q water washing (until the filtrate pH was ~10 to confirm the removal of excess Na without dissolving the zeolite), and drying in an oven at 80 °C (to remove excess water without causing thermal damage to the samples). Finally, the dried zeolites were equilibrated in a desiccator, with saturated $CaCl_2$ solution and CO_2 trap placed inside to maintain a constant 35% relative humidity and low CO_2 level, respectively. It was observed, that the formation of hydrosodalite was strongly preferred under highly alkaline synthesis conditions (at H_2O/Na_2O molar ratio < 38, see Figure A1), while an increase of the amount of water (the molar ratio of raw materials

used was $3Na_2O{\cdot}Al_2O_3{\cdot}2SiO_2{\cdot}152H_2O$) resulted in low-silica gismondine P(Na) with the least amount of impurities. For the synthesis of analcime different molar ratios of raw materials were explored to obtain the pure phase, as the alkali, Si, and Al sources used were different from those in literature [29] and had different reactivity. Hydroxycancrinite ($Na_8Al_6Si_6O_{24}(OH)_2{\cdot}2H_2O$) often existed in the solid products [30], as confirmed by XRD (Figure A2). Finally, the molar ratio of SiO_2 to Al_2O_3 was adjusted to 5.2.

Table 1. Experimental conditions for the hydrothermal synthesis of zeolites.

Zeolite	$Na_2O(+K_2O)/Al_2O_3$	SiO_2/Al_2O_3	Al and Si sources	Seeding	SDA/Al_2O_3	H_2O/Al_2O_3	time [a] / h	t [b] / °C
Analcime: ANA	6.5	5.2	$NaAlO_2$ Na_2SiO_3	No	6.1 TEOA [c]	380	24	200
Low-silica P-Na: LS-P(Na) [d]	3	2	$NaAlO_2$ SSS [e]	No	No	152	192	100
Phillipsite-NaK: PHI(NaK)	1.53 (+0.44)	5	$NaAlO_2$ Fumed SiO_2	No	No	82.7	168	100
Phillipsite-Na: PHI(Na)	Na+ exchanged product from PHI(NaK)							
Linda type A: LTA [f]	8.12	2.5	$NaAlO_2$ SSS [e]	No	No	190	2	100
Molecular sieve 4Å: 4 Å	Commercial zeolite from Sigma Aldrich							
Hydrosodalite: SOD(OH)	4	2.0	$NaAlO_2$ SSS [e]	No	No	76	192	100
Sodalite: SOD(Cl) [g]	8.12	2.5	$NaAlO_2$ SSS [e]	No	No	190	2	100
Cancrinite-NO_3: CAN(NO_3) [h]	8.12	2.5	$NaAlO_2$ SSS [e]	No	No	190	2	100
Chabazite-Na: CHA(Na)	2.67 (+0.89)	7	Fresh $Al(OH)_3$ HS-40 [i]	No	0.04 TMA-OH [j]	110	168	95
Faujasite-X: FAU-X	16	8	$NaAlO_2$ SSS [e]	No	No	650	20	90
Faujasite-Y: FAU-Y	4	8.1	$NaAlO_2$ HS-40 [i]	No	No	120	60	80
Natrolite: NAT	8	10	Geloxal10 AS-40 [k]	10% SCO [l]	No	150	120	150
Mordenite-Na: MOR(Na)	6	30	$NaAlO_2$ Fumed SiO_2	5% MOR	No	780	24	170

[a] Crystallization time; [b] Crystallization temperature; [c] triethanolamine; [d] Mixing the raw materials at 60 °C [25]; [e] sodium silicate solution; [f] Incubation for 3 h at 70 °C without stirring

before crystallization at 100 °C; [g] Additionally introducing 3 molar proportions of NaCl; [h] Additionally introducing 3 molar proportions of $NaNO_3$; [i] aqueous colloidal silica HS-40; [j] tetramethylammonium hydroxide pentahydrate; [k] aqueous colloidal silica AS-40; [l] scolecite.

The Na^+-endmembers of the as-synthesized phillipsite and chabazite, which contained mixed extra-framework cations (i.e., Na^+ and K^+), were prepared by hydrothermal cation exchange method [31], using 3.0 M NaCl solution as the exchange solution. Typically, a solid-to-liquid (S/L) ratio of 50 g L^{-1} was used. The suspensions were sealed in a Teflon vessel and placed in an oven at 80 °C for 24 h. After the exchange reaction, the suspensions were centrifuged and the remaining solids were washed with Milli-Q water one time. In order to obtain a pure enough Na^+-endmember (further confirmed by energy-dispersive X-ray spectroscopy (EDS) results in Section 3.1.2), this process was repeated 3 times. In the last cycle, the solid product was collected by vacuum filtration and washed by Milli-Q water for 4 times to remove the residual NaCl. The drying and storage methods were then the same as described above. By these methods, 12 types of Na-based zeolites were synthesized, belonging to six different secondary building units (SBUs) groups.

2.3. Solid phase characterization

The framework structures of zeolites were identified by XRD. XRD and Fourier transformed infrared (FT-IR) were also used to confirm the identity of the zeolite, while the bulk element compositions were determined by scanning electron microscopy (SEM) and EDS, partially combined with acid digestion. The water contents of zeolites were obtained from the weight loss observed by TGA-DTA.

The zeolites were ground and passed through a 63 μm sieve before XRD measurements to check their purities and any possible competing crystalline phase. XRD patterns were collected with a PANalytical X'Pert Pro diffractometer in a θ-2θ configuration. The step size, scan speed, and range were 0.017° 2θ, 0.54 s, and 5-90° 2θ, respectively. Oriented mounts were prepared and Co Kα radiation at 1.789 Å used.

192 TGA was performed with a Mettler Toledo TGA/SDTA 851e on ~40 mg of sample using a
193 heating rate of 20 °C min^{-1} from 30 to 980 °C and N_2 as protective gas. Prior to performing
194 TGA, samples were equilibrated in a CO_2- controlled desiccator at 35% relative humidity (us-
195 ing a $CaCl_2$ solution) for at least one week, in order to unify the adsorbed water content on all
196 the zeolites.

197 FT-IR spectra were collected in the mid-region (3996 to 339 cm^{-1}) on a Bruker Tensor 27 FT-
198 IR spectrometer using the attenuated total reflection (ATR) technique on small amounts (~5
199 mg) of powdered sample. Spectra were corrected with background subtraction and normalized
200 by the maximum absorbance of asymmetrical stretch of Si-O(Si/Al) bands.

201 The morphology and elemental fraction of zeolites were characterized by SEM and EDS anal-
202 yses, respectively, which were carried out with a Philips ESEM FEG XL 30. Powder samples
203 were used to characterize the morphology, while pressed zeolite pellets, with relatively flat
204 surfaces were used for the analysis of elemental fraction. In both cases, samples were placed
205 on carbon discs. A beam voltage of 15 kV and the carbon coating were chosen for EDS analy-
206 sis. The composition of selected zeolites (ANA, PHI(NaK), LTA, FAU-X, and NAT) was
207 also obtained from chemical analysis of the samples digested in concentrated HCl, which
208 agreed well with the SEM/EDS composition verifying both the accuracy of the EDS method
209 and the high quality of the synthesized target zeolites (Table A1).

210 **2.4. Batch dissolution experiments**

211 First, the dissolution kinetics of several selected zeolites (FAU-X, FAU-Y, ANA, and LS-
212 P(Na)) were studied at 20 ℃ by sampling after 30, 72, and 138 days of dissolution. Each type
213 of zeolite was dispersed into ultrapure water with an identical S/L ratio of 50 g L^{-1}. Once the
214 equilibrium time was confirmed, batch dissolution experiments were conducted at 20, 50, 60,
215 and 80 ℃, in order to obtain solution composition data from which the solubility products
216 (K_{sp}) were calculated for all zeolites at different temperatures. The suspension was passed

through 0.22 μm syringe Nylon filters after equilibrating for 30 days. The same day, a small aliquot of the filtrate for each reactor was extracted and was measured at laboratory temperature using a Knick pH meter (pH-Meter 766) and a Knick SE100 electrode. Another portion of the filtrate was diluted with Milli-Q water as necessary and the total aqueous concentrations of Na, K, Ca, Al, Si, Cl and N were analyzed by ion chromatography (IC, Dionex DP series ICS-3000) on the same day. The experimental detection limit of the IC was estimated to be 0.025 mg L^{-1} for all elements and the IC measurement error 5-10%.

2.5. Thermodynamic modelling

Thermodynamic modelling was carried out using the Gibbs free energy minimization program GEM-Selektor v3.3 [32], a powerful geochemical modelling code that computes the equilibrium speciation and the amount of both aqueous and solid phase in a complex chemical system using Gibbs free energy minimization algorithms. General thermodynamic data for aqueous, solid, and gaseous species were taken from the PSI-GEMS thermodynamic database [33]. The cement database Cemdata'18 [20], and the C-N-A-S-H model from [34], was used for cement minerals. Data for albite were taken from the SUPCRT database [17].

In order to draw the predominance diagrams for the cement-zeolite-clay system, the PHREEQC (Version 3) [35] and PhreePlot codes (Version 1) [36], coupled to the PHREEQC database version of Cemdata'18, the thermodynamic data for clay minerals in the THERMOCHIMIE database [37], and the generated thermodynamic data for zeolites, were employed. Note that the thermodynamic data in Cemdata18 and in THERMOCHIMIE are not fully consistent; to minimize inconsistencies, the $\log K_{sp}$ as given in THERMOCHIMIE were used. The "hunt and track" algorithm (i.e., ht1) was used for finding field boundaries of most abundant minerals.

240 The activity of a species i, {i}, was calculated using GEMS from the measured concentrations
241 using $\{i\} = \gamma_i \cdot m_i$, where γ_i is the activity coefficient and m_i is the concentration in mol kg^{-1}
242 H_2O. Values of γ_i were computed with the built-in extended Debye-Hückel equation:

243 $$\log \gamma_i = \frac{-A_y z_i^2 \sqrt{I}}{1 + B_y a_i \sqrt{I}} + b_y I \qquad (1)$$

244 where the ion size parameter a_i = 3.31 Å is assigned a common value for all charged ions and
245 b_y = 0.098 in NaOH solutions at 25 °C, z_i denotes the charge of species *i*, I is the effective mo-
246 lal ionic strength (M), and A_y and B_y are P,T-dependent coefficients. This activity correction
247 is thought to be applicable up to ~1 M ionic strength [38]. For neutral species, $z = 0$ and
248 Equation (1) simplifies to the Setschenow equation [39]: $\log \gamma_i = b_\gamma I$. The activity of water is
249 in GEMS directly calculated from its mole fraction: $\log \gamma_{H2O} = \log (x_{H2O,w} / X_w)$, where X_w is
250 the total mole quantity of the aqueous phase (including water-solvent).
251 The activities of aqueous species $\{Na^+\}$, $\{K^+\}$, $\{Ca^{2+}\}$, $\{AlO_2^-\}$, $\{SiO_2^0\}$, $\{Cl^-\}$, $\{NO_3^-\}$,
252 $\{OH^-\}$, and $\{H_2O\}$, were used to calculate the solubility products, K_{sp}, for zeolites at 20, 50,
253 60, and 80 °C according to the corresponding stoichiometric composition of the different zeo-
254 lites. The Gibbs free energy of reaction, $\Delta_r G^0$ (J/mol), to describe the dissolution reaction of a
255 zeolite can be calculated from K_{sp}:

256 $$\Delta_r G^0 = -RT \ln K_{sp} = \Sigma_i \nu_i \Delta_f G_i^0 \qquad (2)$$

257 where R = 8.31451 J/mol/K and T is absolute temperature in K. The Gibbs free energy of for-
258 mation, $\Delta_f G^0$ (J/mol) of a zeolite can then be calculated from Equation 2. ν_i is the stoichio-
259 metric reaction coefficient and $\Delta_f G_i^0$ (J/mol) refers to $\Delta_f G^0$ (J/mol) of the species used in the
260 dissolution reaction.
261 The apparent Gibbs free energy of formation, $\Delta_a G_T^0$ (J/mol), can be calculated at the tempera-
262 ture of interest using:

$$\Delta_a G_T^0 = \Delta_f G_{T_0}^0 - S_{T_0}^0 (T - T_0) + \int_{T_0}^{T} C_P^0 dT - \int_{T_0}^{T} \frac{C_P^0}{T} dT \quad (3)$$

where T_0 is equal to 298.15 K, S^0 the standard entropy in J/mol K, and C_p^0 the standard heat capacity in J/mol/K. Assuming that C_p^0 [40] is a constant over the narrow temperature interval studied (20 – 80 °C), the integral terms in Equation (3) can be solved to give:

$$\Delta_a G_T^0 = \Delta_f G_{T_0}^0 - S_{T_0}^0 (T - T_0) - C_p^0 (T \ln \frac{T}{T_0} - T + T_0) \quad (4)$$

A more detailed description of the derivation of the dependence of the Gibbs free energy on temperature is given in [19] and [41].

C_p^0 values for the zeolites were selected from experimentally measured C_p^0 values in the literature when their frameworks and compositions were nearly identical; if not available, they were estimated using the additivity method [17-19] based on a reported experimental C_p^0 value of zeolite having the same framework and/or on the elementary (hydro)oxide components assuming $\Delta C_{p,r} = 0$. Also the entropy values were taken if possible from the literature or calculated from structurally similar zeolites according to the procedure outlined in [17].

S^0 of the target zeolite was calculated from the entropy of the elementary (hydro)oxide components and of the zeolite with the same framework assuming $\Delta S_r^0 = 0$ considering the molar volume (V^0, in cm^3/mol) according to Eq. 62 in [17]:

$$S^0 = \frac{\sum \nu_i S_i^0 (\sum \nu_i V_i^0 + V^0)}{2 \sum \nu_i V_i^0} \quad (5)$$

Where ν_i represents the stoichiometric number of the *i*th elementary component in the chemical formula of the target zeolite; S_i^0 and V_i^0 are the standard entropy and molar volume, respectively, of the *i*th elementary component. Only the S^0 value of LS-P(Na) that was determined independently by fitting the log K_{sp} data as a function of temperature with the assistance of the GEMS-Selektor code. The polymer model described by [13] was also tried but the resulting S^0 values had larger difference with our experimental solubility products

compared to that with the additivity method. For the additivity method, the thermodynamic data of the elementary (hydro)oxide components (i.e., NaOH, $Ca(OH)_2$, KOH, $Al(OH)_3$, SiO_2, NaCl, $NaNO_3$, and Na_2CO_3) was extracted from [42, 43] and summarized in Table A2. Instead of free H_2O, zeolitic H_2O was adopted in the calculation, with S^0 and C_p^0 values of 59.0 and 47.7 J/mol/K, respectively [17]. The V^0 values of zeolites were calculated from the indexed PDF cards that matched well with our experimental XRD data. Slight differences in composition and the effect this may have on V^0 values were ignored.

3. Results and discussion

3.1. Characterizations of zeolites

3.1.1. Zeolite SBUs and frameworks

The XRD patterns of the investigated zeolites are summarized in Figure 1, where they were plotted according to their SBU groups. The primary building block of the zeolite structure is a tetrahedron of four oxygen atoms surrounding a central Si atom (SiO_4), which are connected through shared oxygen atoms to form a wide range of small SBUs. Different combinations of the same SBU may give numerous distinctive structural polyhedra formed from smaller ring units and zeolites are often classified based on SBUs contained in the structure. In the present study zeolites with a singly connected 4-ring structure (S4R: ANA, LS-P(Na), PHI(Na), and PHI(NaK)), with a doubly connected 4-ring structure (D4R: LTA and 4Å), with a singly connected 6-ring structure (S6R: SOD(OH), SOD(Cl), and CAN(NO_3)), with a doubly connected 6-ring structure (D6R: CHA(Na), FAU-X, and FAU-Y), with a 4=1 structure (NAT), and with a 5-1 structure (MOR(Na)) were synthesized and studied. Most of the zeolites were pure and no impurities were observed except for LS-P (Na). In LS-P (Na), in addition to LS-P (Na) a very small amount of SOD(OH) and LTA were detected, which have the same Si/Al molar ratio.

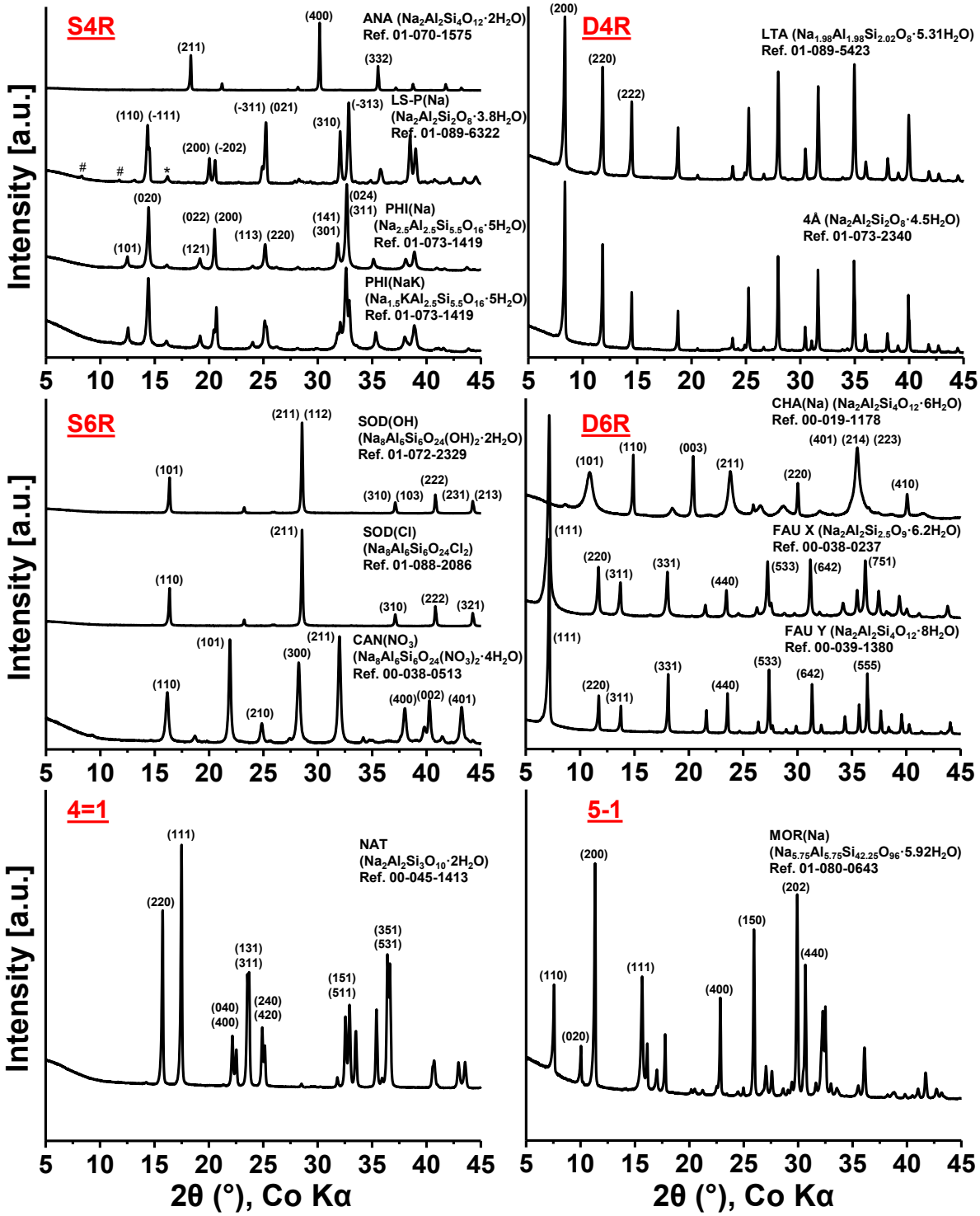

Figure 1. Powder XRD patterns of the synthesized Na-based zeolites. For each pattern, the identified phase component with PDF reference card number is attached on the top right. Only the diffraction peaks of impurities are marked with #: LTA and *: hydrosodalite, while all the other peaks are attributed to the pure zeolite phases.

Zeolites having the same SBU often show a certain similarity on their XRD patterns, e.g., LS-P and PHI in the S4R group, indicating that the short-range ordering strongly affected the

long-range ordering. The comparison of the XRD patterns of PHI, where only Na is present, with PHI(NaK), where both K and Na are present, shows that the structure symmetry increased when the cavity was occupied by Na^+ only as indicated by the absence of peak splits at ~20.5, 25.2, and 32.0 ° 2θ.

In D4R group, the commercial molecular sieve of zeolite 4Å had almost the same XRD pattern as LTA. SOD(OH), SOD(Cl), and CAN(NO_3) are built with the same SBU (i.e., S6R), resulting in very similar XRD patterns as well. In the D6R group, FAU-X and FAU-Y have the same framework structure and thus nearly indifferentiable patterns, with almost the same 2θ angle positions but slightly different ratios of peaks intensity. According to their Si/Al molar ratio, FAU zeolites are generally classified into X type (having a ratio between 1 and 1.5) and Y type (above 1.5) [44]. CHA(Na) showed quite different patterns although it also belongs to the D6R group.

The synthesized natrolite, classified in the 4=1 group, shows a high phase purity. As reported by [23], Natrolite has ordered Si and Al T-sites distribution in orthorhombic symmetry, and can form at longer crystallization times from tetranatrolite, which has completely disordered T-sites in tetragonal symmetry. The transformation of tetranatrolite to natrolite can be verfied by the split of XRD peaks at ~22.3, 23.5, 25.0, 32.5, and 36.5° 2θ. The almost complete peak splits in our work indicated a well ordered T-sites distribution in the highly crystalline NAT structure. Besides, highly pure Na-based mordenite, belonging to 5-1 SBU group, was synthesized successfully, showing the strongest diffraction peak from its crystal face of (200). Secondary electron images of the zeolites, shown in Figure A3, showed the typical 3-D structures of the zeolites and confirmed the absence of other phases. The framework types of zeolites can be easily identified by XRD as shown above. However, zeolites with the same framework type may have different contents of Si, Al, and extra-framework cations, and can still result in very similar diffraction patterns.

3.1.2. Elemental composition

The bulk element compositions of Na, Al and Si in the synthesized zeolites were determined by SEM-EDS on flattened samples. The atomic percentages of the heavier elements ($Z \geq 11$) are listed in Table 2. The molar ratio of the positive extra-framework charge number to the aluminum substitution, represented by Cat/Al, should be equal to one in a perfect aluminosilicate zeolite structure. As shown in Table 2, most of the Cat/Al values were approximately equal to 1, except for SOD(Cl) and zeolite 4Å.

For SOD(OH) and CAN(NO_3), it was assumed that the respective extra-framework OH^- and NO_3^-, which are too light to be analyzed reliably by EDS, were equal to one-quarter of Na in mole according to the XRD analysis. Considering the estimated molar fraction of OH^- and NO_3^-, the Cat/Al ratios of SOD(OH) and CAN(NO_3) were calculated to be 1.03 and 1.04, respectively, which were reasonable for the zeolite structure. The Cat/Al ratio of SOD(Cl) was 0.17 more than 1.00, indicating the existence of ~1.61 atomic percentage (at.%) of OH^-. The OH^- partly coupled with Na^+ and partly acted as the extra-framework anion for charge balance of zeolite structure.

The commercially available zeolite 4Å, characterized as a Type A zeolite ($Na_2Al_2Si_2O_8 \cdot 4.5H_2O$) by XRD, had Si/Al ratios of ~1.3, which was larger than expected for Type A zeolite. This could be explained by the possible existence of non-framework Si such as amorphous silica and by the possible substitution of Si^{4+} by non-Al^{3+} cations such as Fe^{3+}; if all the cations in zeolite 4Å were counted as the charged extra-framework ions, the whole zeolite structures would be positively charged (Cat/Al ratios of zeolite 4Å were 1.31). The TGA data (Figure 2) indicate that surplus of cations are probably present as carbonates. The composition of the zeolite 4Å phase is here taken as $Na_2Al_2Si_2O_8 \cdot 4.5H_2O$; the presence of amorphous SiO_2 and carbonates contributes to the relatively low water content of 18.3% observed by TGA (Table 3) instead of the theoretical 19.9%.

The EDS results indicated that PHI(Na), the cation exchanged zeolite, still contained a small fraction of the previous host cation (i.e., K^+), suggesting that complete cation exchange was not reached. Thus, a chemical formula of PHI(Na) was calculated to be $Na_{2.3}K_{0.2}Al_{2.5}Si_{5.5}O_{16}{\cdot}5H_2O$. The Si/Al ratio of MOR(Na) was determined to be 7.43, which was very close to the value (i.e., 7.35) obtained from XRD characterization. Overall, the elemental fractions obtained from EDS analysis agreed well with the XRD results, confirming the expected chemical compositions of the various zeolites.

Table 2. Atomic percentages of selected elements of zeolites. The ratio of positive extra-framework charge number to negative framework charge number (Cat/Al) was calculated and the molar ratio of Si to Al listed as well.

Zeolite	Na at.%	Al at.%	Si at.%	K at.%	Ca at.%	Fe at.%	Mg at.%	Cl at.%	Cat/Al	Si/Al
ANA	7.50	7.95	15.21						0.94	1.91
LS-P(Na)	10.31	10.26	10.54						1.00	1.03
PHI(Na)	6.62	7.06	14.75	0.58					1.02	2.09
PHI(NaK)	3.99	6.29	12.91	2.54					1.04	2.05
LTA	10.20	10.69	11.06						0.95	1.03
4Å	8.09	8.48	11.47	0.05	0.20	0.27	1.06		1.31	1.35
SOD(OH)	13.21	9.53	9.67						1.03	1.01
SOD(Cl)	13.49	9.47	9.92					2.38	1.17	1.05
CAN(NO_3)	12.92	9.31	9.96						1.04	1.07
CHA(Na)	6.33	6.47	12.65						0.98	1.96
FAU-X	8.82	9.35	12.12						0.94	1.30
FAU-Y	7.67	7.65	14.49						1.00	1.89
NAT	8.16	7.91	11.57						1.03	1.46
MOR(Na)	3.15	3.06	22.70						1.03	7.43

3.1.3. Water content

All the zeolite powder was characterized by TGA-DTG analysis, in order to quantify the water content and to check possible contaminations and carbonation during the synthesis. As shown in Figure 2, the TGA-DTG curves of the zeolites were also grouped based on the SBU group. All zeolites, with the exception of natrolite, analcime, cancrinite and sodalite, lost most water at relatively low temperatures, between 100 and 300°C, consistent with the presence of

water within the cavities of the zeolites. Zeolites with the same framework type showed in many cases a similar water loss pattern. Zeolite 4Å has an LTA framework and has thus a very similar water loss pattern. However, less relative weight loss was obtained for 4Å probably due to the presence of some amorphous silica as deduced from the EDS results. FAU-X and FAU-Y, which were synthesized at 80 and 90 °C, showed both similar dehydration temperatures and approximately equal weight losses (Table 3). In general, it was found that the temperatures for the main dehydration peaks increased with the crystallization and thus synthesis temperatures of the synthesized zeolites. The temperatures of the main dehydration peaks are in the order of LTA = PHI (Na) = PHI (NaK) (all the three were synthesized at 100 °C) < NAT (synthesized at 150 °C) < ANA (synthesized at 200 °C). MOR(Na), whose dehydration peak located at around 100°C, was the exception, indicating that the zeolite dehydration temperature is related to both the crystallization temperature as well as to the size of the channels within the zeolitic structure.

LS-P (Na), the gismondine (GIS) type zeolite, shows at least three DTGA peaks of dehydration in the region of 120-350 °C (Table 3), in good agreement with previous reports [45, 46]. Natural gismondine often has quite complex thermal behavior and several types of extraframework cations, whose water molecules are distributed on six sites in their structural refinement [47]. Compared to the natural gismondine, our synthesized GIS type zeolites have smaller sizes, only one type of cation, more simplified water distribution environment, and thus less dehydration steps. Similar phenomenon was observed for PHI (Na) and PHI (NaK). PHI(Na), having a single type of cation (Na^+), exhibited fewer dehydration steps than PHI(NaK), which has both Na^+ and K^+ in cages. Na^+ is more hydrophilic than K^+ and can attract more water molecules, leading to slightly more water loss for PHI(Na) than for PHI(NaK).

409 Cancrite and sodalite showed weight losses also at higher temperatures. For CAN(NO_3) the
410 weight loss above 700°C was attributed to denitration according to equation (6)

411 $2NaNO_3 \rightarrow Na_2O + NO + NO_2 + O_2$ ($t > 700$ °C) (6)

412 as previously reported [48]. The nitrate content of 10.4% obtained from the weight loss at
413 above 700°C was in agreement with the theoretical value of 9.9%. In SOD(Cl) the anionic
414 sites should be mainly occupied by Cl^-, as confirmed by the dechloridation peak at 680 °C in
415 the DTGA, and was supported by XRD and EDS results. In the DTGA curve of SOD(Cl), a
416 broad peak attributed to the dehydroxylation was observed at 370 °C, indicating the existence
417 of some OH^- in the extra-framework. The small portion of OH^- was likely structurally intro-
418 duced during the hydrothermal synthesis under the high pH conditions used during hydrother-
419 mal synthesis. For SOD(OH), the total relative weight loss (7.3%) from both dehydration and
420 dehydroxylation was well matched with the corresponding theoretical value (7.2%); some car-
421 bonation was detected at 750 °C, promoted by the high alkalinity of the synthesis gel of
422 SOD(OH). The commercial 4Å was also slightly carbonated, showing a decarbonation peak at
423 around 660 °C. As shown in Figure 2, no carbonation was detected for any of the other syn-
424 thesized zeolites.

425 For MOR(Na), 11.46% was adopted: $Na_{0.72}Al_{0.72}Si_{5.28}O_{12}\cdot 2.71H_2O$ as the relative weight loss
426 of water as its theoretical value, ~3.42% based on the XRD analysis, showed a profound dis-
427 crepancy with the value obtained experimentally from TGA-DTG analysis. Overall, the ex-
428 perimental relative weight loss of each zeolite was in accordance with the theoretical value
429 based on the chemical formula indicated in the PDF reference card (Table 3).

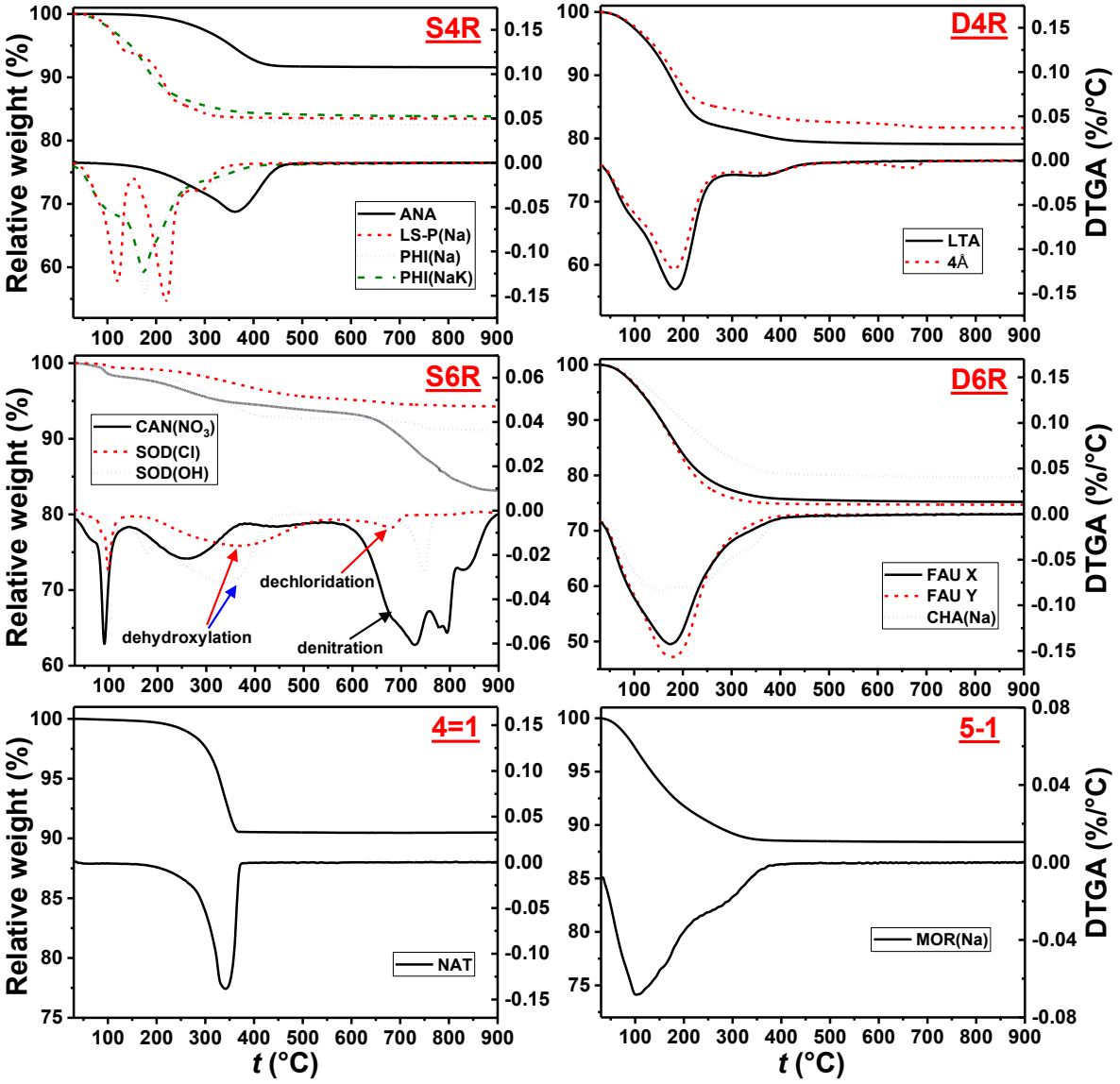

Figure 2. TGA-DTG curves of the synthesized Na-based zeolites.

Table 3. Summary of the theoretical relative weight loss derived from XRD analysis and the experimental value obtained from TGA-DTG of each zeolite. Temperatures of the main DTGA peaks were listed as well. The weight loss that was not attributed to dehydration is plotted in italic.

Zeolite	Theoretical relative weight loss	Experimental relative weight loss / DTGA peak position
ANA ($Na_2Al_2Si_4O_{12}·2H_2O$)	8.18%	8.29% / 362 °C
LS-P(Na) ($Na_2Al_2Si_2O_8·3.8H_2O$)	19.4%	16.3% / 121, 221, 288 °C
PHI(Na) ($Na_{2.5}Al_{2.5}Si_{5.5}O_{16}·4H_2O$)	14.4%	17.1% / 178 °C
PHI(NaK) ($Na_{1.5}KAl_{2.5}Si_{5.5}O_{16}·4H_2O$)	14.0%	15.7% / 178 °C
LTA ($Na_{1.98}Al_{1.98}Si_{2.02}O_8·5.31H_2O$)	25.5%	20.7% / 183, 353 °C
4Å ($Na_2Al_2Si_2O_8·4.5H_2O$)	-	18.3% / 180, 372 °C
SOD(OH) ($Na_8Al_6Si_6O_{24}(OH)_2·2H_2O$)	3.72% *3.51%* -	7.29% in total / 75.5 and 180 °C *344 °C (dehydroxylation)* *1.19% (decarbonation)*
SOD(Cl) ($Na_8Al_6Si_6O_{24}Cl_2$)	- - 7.32%	0.69% / 87.1, 98.9 °C (surface water) *4.84% / 373 °C (dehydroxylation*) *5.78% / 682 °C (dechloridation)*
CAN(NO_3) ($Na_8Al_6Si_6O_{24}(NO_3)_2·4H_2O$)	6.58% 9.87%	6.48% / 91.0, 264, 444 °C *10.4% / above 728 °C (denitration)*
CHA(Na) ($Na_2Al_2Si_4O_{12}·6H_2O$)	21.1%	20.2% / 158, 224 °C
FAU-X ($Na_2Al_2Si_{2.5}O_9·6.2H_2O$)	26.2%	24.5% / 174 °C
FAU-Y ($Na_2Al_2Si_4O_{12}·8H_2O$)	26.3%	25.1% / 178 °C
NAT ($Na_2Al_2Si_3O_{10}·2H_2O$)	9.48%	9.47% / 341 °C
MOR(Na) ($Na_{0.72}Al_{0.72}Si_{5.28}O_{12}·2.71H_2O$)	-	11.5% / 102 °C

3.1.4. FT-IR analyses

FTIR transmittance spectra and the corresponding 2nd derivative spectra of the zeolites, with wavenumbers ranging from 1400 to 340 cm^{-1}, were classified into six subgroups based on the SBUs and are shown in Figure 3. The 2nd derivative spectra can help identifying the positions

of broad vibration peaks more clearly. The vibration features of the aluminosilicate frameworks of zeolites are mainly visible in the mid and far infrared, especially below 1400 cm^{-1}. The spectra in the wavenumber range from 4000 to 1250 cm^{-1} (Figure A4) typically showed the stretching and bending vibration bands of H-O-H (in H_2O) at ~3350 and 1630 cm-1, respectively, with the former typically giving a broad peak envelop (except for NAT and MOR(Na) that showed several stretching vibrations) and the latter a relatively sharp peak. For CAN(NO_3) the strong and sharp peak appearing at 1427.2 cm^{-1} (less intense signal at 1379.0 cm^{-1}) belonged to the stretching vibration band of N-O in NO_3^-. A summary of the vibration peak wavenumbers of FTIR spectra is shown in Table 4. The IR transmittance bands can be generally separated into two groups: 1) internal vibrations of the TO_4 tetrahedra (i.e., SiO_4 or AlO_4), including asymmetrical stretch (ν_{as}) at 1250 – 920 cm^{-1}, symmetrical stretch (ν_s) at 720 – 650 cm^{-1}, and T-O bend (δ) at 500 – 420 cm^{-1}; 2) external vibrations of linkages, including ν_{as} at 1150 – 1050 cm^{-1}, ν_s at 820 – 750 cm^{-1}, ring vibrations at 650 – 500 cm^{-1}, and pore opening vibrations at 420 – 300 cm^{-1} [49].

Similar features of IR spectra were observed for zeolites having the same SBU. For instance, vibration peaks at approximately 1100, 1030, 740, 670, 600, 430 cm^{-1}, attributed to ν_{as} T-O(T) - Ex, ν_{as} T-O(T) - In, ν_s T-O(T) - Ex, ν_s T-O(T) - In, Ring - Ex, and δ T-O - In, respectively, for the zeolites in S4R group. The similarity of IR spectra was also obvious for the other SBU groups, indicating that the framework vibrations of zeolites can be detected with these IR bands. The ν_{as} bands of FAU-Y are located at higher wavenumbers than that of FAU-X, as FAU-Y has a higher Si/Al ratio and the electronegativity of Si^{4+} is stronger than that of Al^{3+}. The same tendency of band shift was observed for SOD(OH) and SOD(Cl), resulting from the electronegativity difference of extra-framework anions. Overall, the wavenumbers of the main IR bands for each SBU group were in good agreement with the literature values e.g. [50, 51], indicating that the targeted zeolites were collected successfully.

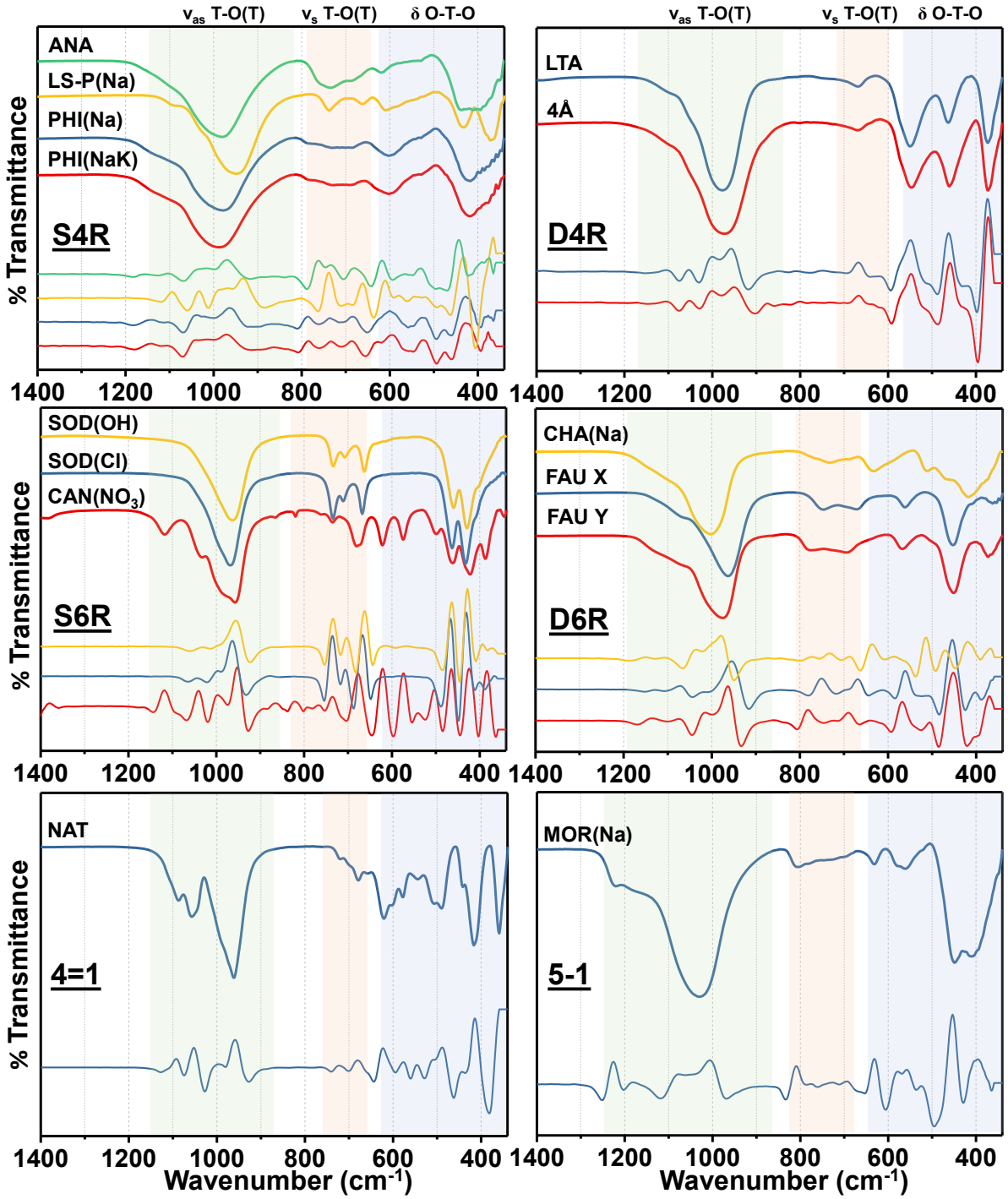

Figure 3. FTIR transmittance spectra of each SBU group of zeolites, with the corresponding 2nd derivative spectra plotted below.

Table 4. Summary of the vibration peak wavenumbers (cm^{-1}) of FTIR spectra for the Na-based zeolites[a].

SBU group	Zeolite	ν O-H	δ O-H	ν_{as} T-O(T) - Ex	ν_{as} T-O(T) - In	ν_{s} T-O(T) - Ex	ν_{s} T-O(T) - In	Ring - Ex	δ T-O - In	Pore - Ex
S4R	ANA	3379	1634	1105	1016, 970	762, 735	681	617, 530	442	
	LS-P(Na)	3330	1639	1094	1034, 934	739	662	611	432	364
	PHI(Na)	3395	1638	1140, 1105	1038, 964	785, 737	685	600, 527	428	
	PHI(NaK)	3416	1638	1142, 1107	1042, 970	785, 733	687	596, 525	428	
D4R	LTA	3379	1649	1105, 1053	999, 957		667	550	463	374
	4Å	3340	1643	1105, 1051	1001, 951		667	548	459	372
S6R	SOD(OH)	3350	1645		1034, 957	735	704, 662		463, 428	
	SOD(Cl)	3350	1653		1043, 997, 964	735	706, 667		467, 430	
	$CAN(NO_3)$[b]	3350	1628	1119	1040, 997, 953	735	677	621, 575, 503	465, 424	384
D6R	CHA(Na)	3396	1643	1151, 1107	1036, 978	773, 733	689	636, 515	471	418, 368
	FAU-X	3381	1645	1128, 1072	955	750	669	561	453	
	FAU-Y	3398	1641	1136, 1074	1014, 962	781	690	567, 505	451	370
4=1	NAT	3537, 3321, 3219, 3175	1632	1092, 1053	995, 959		723, 681	623, 577, 546, 507	488, 444	415
5-1	MOR(Na)	3620, 3410	1628	1076	1227, 1180, 1007	811		631, 577, 557, 525	453	395

[a] ν_{as}, asymmetric stretching vibrations; ν_{s}, symmetric stretching vibrations; δ, bending vibrations; T, Si/Al tetrahedron; Ex, external linkage; In, internal tetrahedra; Ring, ring vibrations; Pore, pore opening vibrations. [b] The stretching vibration peaks attributed to N-O were at 1427.2 and 1379.0 cm^{-1}.

3.2. Thermodynamic properties of Na-based zeolites

3.2.1. Solubility products

The dissolution kinetics of FAU-X, FAU-Y, ANA, and LS-P(Na) at 20 °C were studied and the results are shown in Figure A5. After 30 days of dissolution, the solubility product (log

498 K_{sp}) of each zeolite was not significantly different from the values after 72 and 138 days, sug-
499 gesting that the zeolite dissolution is near equilibrium after 30 days.

500 Based on the corresponding dissolution reaction listed in Table A3, the log K_{sp} values of each
501 studied zeolite at different equilibrium temperatures were calculated and shown in Table 5,
502 together with the aqueous concentrations and pH values. Typically, the IC measurement has
503 errors of 5-10%. The 10% error of the IC measurement will give errors of 0.9-1.5% on the log
504 K_{sp} values. In order to evaluate the systematic error of the whole dissolution experiment, re-
505 peated dissolution experiments were performed on five selected types of zeolites (ANA, LS-
506 P(Na), FAU-X, FAU-Y, and CAN(NO_3)). The resulting uncertainty percentages ranged from
507 1.1% to 7.1% (Table A4). In this study, a general error of 3% was applied on the log K_{sp} val-
508 ues (Table 5 and 6).

509 For each Na-based zeolite the element concentrations and the resulting log K_{sp} value in-
510 creased with temperature generally, indicating a positive enthalpy for the dissolution reaction.
511 The incompletely Na^+ exchanged phillipsite, i.e., PHI(Na) with a chemical formula of
512 $Na_{2.3}K_{0.2}Al_{2.5}Si_{5.5}O_{16}{\cdot}5H_2O$, still contained minor amount of K^+ in the cage. The solubility of
513 a solid with different ions in the cage can be expressed as a solid solution, as a single solid
514 with both ions present, or as pure end-members containing either Na or K. According to the
515 three models, the Lippmann's total solubility product (ΣΠ) and Ksp values of PHI(Na) were
516 calculated ([52, 53], see details in Text A1) and plotted in Figure A6. The value for the Na^+
517 end member was found to be almost equal to that from the solid solution, while the values
518 given by single solid approach and for the K^+ end member deviated largely, suggesting that
519 $Na_{2.3}K_{0.2}Al_{2.5}Si_{5.5}O_{16}{\cdot}5H_2O$ can be treated as solid solution. Since the log K_{sp} values from the
520 solid solution and the Na^+ end member PHI(Na) were almost equal, the Na^+-endmember form
521 was included in the thermodynamic study. Typically, hydrothermal phillipsite displays a wide
522 range of chemical composition, especially of extraframework cations, making the synthesis

with a single cation infeasible. The synthesis of phillipsite is often facilitated in the presence of K^+ plus Na^+ and/or Ca^{2+} [46]. This also implies that the natural phillipsite should contain more than one type of cation in most cases. Therefore, also the thermodynamic property of PHI(NaK) was investigated individually, in which the amount of Na^+ and K^+ was comparable. As shown in Table 6, the solubility of PHI(NaK) is slightly lower than that of PHI(Na), indicating that the Na/K solid solution of PHI(NaK) should be more stable thermodynamically than PHI(Na).

Table 5. Solution composition and pH of zeolite dissolution experiments at 20, 50, 60, and 80 °C. Experimental log K_{sp} values were calculated and listed. [a]

Zeolite	T °C	pH [c]	$[Na]_{tot}$ mM	$[K]_{tot}$ mM	$[Si]_{tot}$ mM	$[Al]_{tot}$ mM	$[N]_{tot}$ mM	$[Cl]_{tot}$ mM	log K_{sp}
ANA	20	10.61	2.128	bdl	0.6916	0.4878	bdl	bdl	-27.87±0.84
	50	9.77	3.455	bdl	1.200	1.005	bdl	bdl	-24.71±0.74
	60	9.58	3.962	bdl	1.287	1.128	bdl	bdl	-24.18±0.72
	80	9.35	5.091	bdl	1.962	1.562	bdl	bdl	-22.86±0.68
LS-P(Na)	20	10.30	1.842	bdl	0.3836	0.5568	bdl	bdl	-20.00±0.60
	50	9.08	2.831	bdl	0.5358	1.347	bdl	bdl	-17.82±0.53
	60	8.70	3.250	bdl	0.6163	1.688	bdl	bdl	-17.25±0.52
	80	8.22	4.775	bdl	0.6112	2.931	bdl	bdl	-16.39±0.49
PHI(Na)	20	11.01	3.441	0.0011	0.3229	0.1534	bdl	bdl	-41.44±1.24
	50	9.91	5.826	0.0037	0.5716	0.2467	bdl	bdl	-36.03±1.08
	60	9.40	6.422	0.0052	0.6027	0.2628	bdl	bdl	-34.28±1.02
	80	8.98	7.295	0.0077	0.8398	0.3510	bdl	bdl	-32.42±0.97
PHI(NaK)	20	10.98	3.213	0.1562	0.4799	0.1341	bdl	bdl	-40.49±1.21
	50	10.24	3.669	0.2340	0.8632	0.2239	bdl	bdl	-37.01±1.11
	60	9.94	3.822	0.2361	0.9825	0.2381	bdl	bdl	-35.72±1.07
	80	9.62	4.307	0.3791	1.312	0.3664	bdl	bdl	-33.86±1.02
LTA	20	11.80	21.27	bdl	1.596	2.565	bdl	bdl	-18.21±0.55
	50	10.74	21.05	bdl	1.358	3.077	bdl	bdl	-17.01±0.51
	60	10.49	20.39	bdl	1.472	2.690	bdl	bdl	-16.83±0.50
	80	10.08	22.01	bdl	1.838	3.486	bdl	bdl	-16.01±0.48

4Å [b]	20	11.06	23.49	bdl	3.240	0.0282	bdl	bdl	-20.10±0.60
	50	9.85	21.80	bdl	3.518	0.0123	bdl	bdl	-19.52±0.58
	60	9.36	20.47	bdl	3.036	0.0133	bdl	bdl	-19.14±0.57
	80	8.48	17.23	bdl	2.424	0.0220	bdl	bdl	-18.52±0.56
SOD(OH)	20	12.28	26.20	bdl	1.285	1.144	bdl	bdl	-67.33±2.02
	50	11.74	54.58	bdl	2.236	2.280	bdl	bdl	-61.20±1.84
	60	11.45	64.06	bdl	2.573	2.714	bdl	bdl	-59.03±1.77
	80	11.17	78.64	bdl	3.169	3.745	bdl	bdl	-57.41±1.72
SOD(Cl)	20	11.12	21.64	bdl	0.6079	0.0529	bdl	3.0514	-72.10±2.16
	50	10.90	31.31	bdl	1.181	0.6574	bdl	4.2416	-64.00±1.92
	60	10.67	36.07	bdl	1.569	1.096	bdl	4.7609	-60.76±1.82
	80	10.62	46.37	bdl	2.212	1.941	bdl	5.5687	-59.10±1.77
CAN(NO_3)	20	11.28	77.65	bdl	0.4292	1.539	20.24	bdl	-59.95±1.80
	50	10.37	78.55	bdl	0.6696	0.3708	22.89	bdl	-59.93±1.80
	60	10.09	80.40	bdl	0.7774	0.5332	23.05	bdl	-57.61±1.73
	80	9.83	82.06	bdl	1.044	0.9516	27.30	bdl	-55.01±1.65
CHA(Na)	20	8.09	0.8714	bdl	0.1341	0.0026	bdl	bdl	-32.89±0.99
	50	7.17	1.275	bdl	0.2835	0.0507	bdl	bdl	-28.72±0.86
	60	7.07	1.471	bdl	0.3579	0.0911	bdl	bdl	-27.69±0.83
	80	7.10	1.452	bdl	0.5250	0.2452	bdl	bdl	-26.15±0.78
FAU-X	20	10.61	9.678	bdl	0.2569	0.4940	bdl	bdl	-21.83±0.65
	50	9.90	6.725	bdl	0.6106	0.7554	bdl	bdl	-20.28±0.61
	60	9.62	6.874	bdl	0.6407	1.042	bdl	bdl	-19.64±0.59
	80	9.25	7.721	bdl	0.7007	2.076	bdl	bdl	-18.56±0.56
FAU-Y	20	10.11	0.9961	bdl	0.3373	0.0679	bdl	bdl	-29.95±0.90
	50	9.02	1.166	bdl	0.4014	0.2195	bdl	bdl	-27.39±0.82
	60	8.61	1.282	bdl	0.4295	0.2054	bdl	bdl	-27.00±0.81
	80	8.31	1.594	bdl	0.6288	0.4734	bdl	bdl	-25.37±0.76
NAT	20	10.06	1.296	bdl	1.052	0.0065	bdl	bdl	-26.34±0.79
	50	8.54	1.536	bdl	1.074	0.0121	bdl	bdl	-24.61±0.74
	60	8.33	1.544	bdl	1.155	0.0140	bdl	bdl	-24.36±0.73
	80	8.06	1.885	bdl	1.406	0.0259	bdl	bdl	-23.35±0.70
MOR(Na)	20	9.80	0.2219	bdl	0.2847	0.0007	bdl	bdl	-23.12±0.69

50	8.78	0.4855	bdl	0.8051	0.0025	bdl	bdl	-20.64±0.62
60	8.48	0.5534	bdl	1.105	0.0030	bdl	bdl	-19.77±0.59
80	8.00	0.5369	bdl	1.635	0.0077	bdl	bdl	-18.41±0.55

[a] bdl: below detection limit that was approximately 0.025 mg/L for each element. [b] The adopted chemical composition of 4Å is $Na_2Al_2Si_2O_8 \cdot 4.5H_2O$ and thus $[Ca]_{tot}$, $[Mg]_{tot}$, and $[Fe]_{tot}$ are not shown here. [c] pH measured at laboratory temperature (25°C) and corrected to 20°C, 50, 60 and 80°C. The pH differences caused by temperatures were calculated with GEMS, i.e., the pH values (all values were measured at laboratory temperature and were above 8) were corrected +0.16 for 20 °C, -0.74 for 50 °C, -0.98 for 60 °C, and -1.40 for 80 °C.

3.2.2. Thermodynamic data of Na-based zeolites

Based on the measured log K_{sp} values at different temperatures, the Gibbs free energy, $\Delta_f G^{0,}$ at different temperatures could be calculated. Completing these data with measured or calculated data for the heat capacity, C_p^0, and entropy , S^0, data allowed to compute the solubility of the zeolites at 25 °C and its changes with temperature based on Eq. (2)-(4) using GEM-Selektor. The generated standard thermodynamic data of Na-based zeolites based on our experiments are shown in Table 6.

Corresponding thermodynamic properties of the selected zeolites in literatures were reviewed and tabulated in Table 7. As shown in Table 7, quite few solubility products were obtained experimentally and some of the reported log K_{sp} values had several log units difference for the same zeolites, such as for analcime, natrolite, chabazite, and zeolite P. Diverse reasons can be responsible for these large discrepancy, such as differences in their derivation (solubility experiments, calorimetric measurements, or phase relations), varying Si/Cat and Si/Al ratios, different cations in the cages, impure samples and varying crystallinity of the selected zeolites. In Figure 4, the log K_{sp} values of several selected zeolites were compared with the available literature values. Those for other zeolites were shown in Figure 5. The log K_{sp} values of

556 each zeolite were fitted well by the modelling curve that was generated based on the thermo-
557 dynamic data in Table 6.

558 The log K_{sp} values of FAU-X obtained currently agree well with literature values obtained
559 from undersaturation experiments of Sefcik and McCormick [54], while the data calculated
560 from the dissolution study by Cizmek et al. [55] were somewhat lower, which is likely related
561 to the very short equilibration time of only 3 hours used in those experiments. The log K_{sp} ob-
562 tained from oversaturation [56] and [7] are above the curve obtained from undersaturation in-
563 dicating a gap between the solubility reached from over and undersaturation. The same ten-
564 dency was discovered in the case of FAU-Y, a higher solubility for the experiments from
565 oversaturation (even after an equilibration time of 3 years) [7], than those measured here from
566 undersaturation indicating again a gap between the solubility reached from over- and from un-
567 dersaturation. Thus, either the solubility experiment or the precipitation experiment did not
568 reach equilibrium.

569 For CAN(NO_3) the solubility increases as a function of temperature, with the exception of the
570 data point at 20 °C, due to a higher aluminum concentration measured in that sample due to
571 reasons unknown. Similar dissolution results were obtained in the repeated dissolution experi-
572 ment for CAN(NO_3) (Table A4). The experimental S^0 value of CAN(NO_3) estimated from the
573 log K_{sp} curve was 1128 J/mol/K, close to the value of 1149 J/mol/K obtained from the experi-
574 mental S^0 value of CAN(CO_3) [57] using the additivity method. Accordingly, the C_p^0 value of
575 CAN(NO_3) was calculated from the measured C_p^0 value of CAN(CO_3) [57]. As reported by
576 Bickmore et al. [58], the experimental log K_{sp} values of CAN(NO_3) at 89 °C were -59.33 and
577 -53.53, respectively, at pH ~12.4 and ~11.3. The value of -53.53 at pH ~11.3 was closer to the
578 pH values in the CAN(NO_3) dissolution experiments (Table 6) and corresponded precisely to
579 the log K_{sp} curve in the present work. Sodalites, together with cancrinites, are some of the few
580 zeolites, which possess anionic sites in the extraframeworks. However, no solubility study is

581 available for sodalities such that their stability can only be estimated from available enthalpy
582 measurements [59, 60], and entropy data estimated from structurally related zeolites as done
583 in Myers et al. [18].

584 The thermodynamic data of NAT determined in the present study agreed well with the values
585 based on a critical review from Blanc et al. [11], but were clearly less negative than those de-
586 termined in the presence of albite [7]. This might be due to the slow dissolution of albite in
587 these experiments, which led to non-equilibrium conditions; in fact re-measurement of these
588 data after longer equilibration times (6 years) resulted in similar values as reported here [22].

589 In this study, ANA, FAU-Y and CHA(Na) have the same chemical formula (except for the
590 hydrate numbers) but different frameworks. It can be expected the framework largely deter-
591 mines the zeolite solubility. In the investigated temperature range of 20 to 80 °C, ANA was
592 more soluble than FAU-Y and CHA(Na). The ANA framework formed under higher tempera-
593 ture (200 °C) than FAU/CHA (~90 °C) framework, and could be thus expected to be less sol-
594 uble around 200 °C. Assuming that C_p^0 variations with temperature are similar for ANA,
595 FAU-Y and CHA(Na), the extrapolated log K_{sp} curves of the three zeolites (Figure A7) veri-
596 fied that analcime was more stable than FAU-Y and CHA(Na) at 200 °C.

597 In addition, the measured log K_{sp} values for ANA were considerably larger than those re-
598 ported for natural analcime in literatures [11, 13, 61, 62]. As shown in Figure 4e, all the data
599 points and curves were corresponding to an identical chemical composition of
600 $Na_2Al_2Si_4O_{12}{\cdot}2H_2O$, except for the one from Blanc et al. [11] with a chemical formula of
601 $Na_{1.98}Al_{1.98}Si_{4.02}O_{12}{\cdot}2H_2O$. Note that a difference of 0.03 cation per formula unit can result in
602 2 log units difference in the solubility products expressed as log K_{sp} as shown in [11]. The ex-
603 periments for ANA and FAU-Y were repeated and confirmed this observation (Table A4).
604 The solubility data recalculated from the measured concentration in Wilkin and Barnes [62]
605 from natural samples, resulted in roughly 4 log units lower solubility products than those

606 measured in the present work form synthetic samples as shown in Figure 4e. This large differ-
607 ence could be related to either a strongly stabilizing effect of minor elements by an as yet un-
608 determined mechanism on the natural analcime investigated by Wilkin and Barnes [62] or an
609 effect of the synthesis method. In the current work, ANA was synthesized with an assistance
610 of organic template, which could lead to more structural defects and possible organic residues
611 in the synthesized ANA.

612 No experimental solubility data is available in literature for MOR(Na) with the same Si/Al ra-
613 tio and as Na^+-endmember. After normalizing to the same total number of TO_4, the calculated
614 log K_{sp} values from Blanc et al. [11] were plotted in Figure 4f to compare with our experi-
615 mental data. The significant discrepancy was probably due to the different Si/Al ratios and
616 due to the presence of Ca^{2+} as extraframework cation, although the high Si/Al ratio of the
617 mordenite should suppress the effect of extraframework cations as there are little cationic sites
618 in such an aluminosilicate framework [63]. Therefore, the large difference on the solubility
619 behavior should be mainly resulted from the different Si/Al ratios.

620 From a kinetic point of view, the cases of LTA and LS-P(Na) are of specific interest. Both
621 LTA and LS-P(Na) were synthesized at 100 °C with the former phase lasting for 2 h and the
622 latter for 192 h (Table 1). As shown in Figure 5, the log K_{sp} value of LTA is larger than that
623 of LS-P(Na) at 25 °C, indicating that LTA is less stable than LS-P(Na). The log K_{sp} curves of
624 both phases are overlapping between 80 and 100 °C, suggesting that LTA could be more sta-
625 ble at higher temperature and that in the temperature range the equilibration time could be of
626 large importance.

627 In general, the zeolites synthesized in this study have a higher solubility than natural zeolites.
628 Such differences between natural and synthetic zeolites could be related to the presence of mi-
629 nor elements that can stabilize the natural zeolites, to different crystallinity of the zeolites,
630 and/or to smaller crystal sizes of synthetic zeolites. Blanc et al. [11], for instance, derives a 3

631 log units lower solubility for the natural zeolite gismondine than for the synthetic zeolite
632 P(Ca), with the same nominal composition. The solubility discrepancy was especially obvious
633 for analcime. Murphy et al. [64] and Wilkin and Barnes [62] used natural analcime, which
634 could be more stable due to the higher crystallinity than the phase precipitated here and due to
635 the presence of minor phases. Although high crystallization temperature (e.g., 200 °C for
636 ANA) was applied during synthesis and the zeolites showed sharp peaks (i.e., good crystallin-
637 ity) in the XRD patterns, their crystallinity degrees could be still lower and more structural
638 defects that increase solubilty could exist compared to the natural ones. On the other hand, the
639 equilibration time could also affect the results (Figure A5), which could lead to somewhat
640 higher solubility here. For analcime for example, Benning et al. [63] and Murphy et al. [64]
641 used equilibration times up to two years at 25 °C in order to achieve equilibrium from dissolu-
642 tion and precipitation, although the differences in dissolution experiments were small after 3
643 months and longer. In addition, the presence of minor elements in the natural zeolites could
644 stabilize them, compared to the relatively pure synthesized zeolites, which is however, diffi-
645 cult to assess based on the limited amount of experimental data available. Differences in mi-
646 nor elements and/or variation in the composition could also explain the relatively large differ-
647 ence in experimentally determined solubility data for analcime as shown in Figure 4.
648 In contrast, the log K_{sp} values of natrolite determined in the present study compare favorably
649 (Figure 4) with the values derived in Blanc et al. [11] generated from calorimetric measure-
650 ments [65] as well as with recent data of a long-term (6 years) solubility study [22]. In con-
651 trast, the solubility values determined by Lothenbach et al. [7] after 1 and 3 years of equilibra-
652 tion (within the same experimental series as [22]) were considerably lower, indicating that
653 those experiments containing calcium and slowly reacting albite had not been in equilibrium.
654 In the current study, the precipitation/crystallization and dissolution processes investigated
655 can be considered as "young" synthetic Na-based zeolites. Such “immature” zeolites could

evolve to more stable states with time and/or temperature, but as they are synthetic they are also less influenced by the presence of minor elements. The data selected in the present study seem thus well suited to model the precipitation of zeolites over relatively short periods (e.g., during cementitious material hydration or ageing).

Table 6. Standard thermodynamic data of Na-based zeolites at 25 °C, derived in the current study.

SBU group	Zeolite	log K_{sp}	$\Delta_f G^0$ (kJ/mol)	$\Delta_f H^0$ (kJ/mol)	S^0 (J/mol/K)	C_p^0 (J/mol/K)	V^0 (cm^3/mol)
S4R	ANA ($Na_2Al_2Si_4O_{12}·2H_2O$)	-26.8±0.8	-6139.70	-6575.84	469[a]	425[b]	194.84
	LS-P(Na) ($Na_2Al_2Si_2O_8·3.8H_2O$)	-19.6±0.6	-4858.72	-5314.82	374	384[c]	153.49
	PHI(Na) ($Na_{2.5}Al_{2.5}Si_{5.5}O_{16}·5H_2O$)	-39.4±1.2	-8717.83	-9438.72	692[d]	620[d]	304.74
	PHI(NaK) ($Na_{1.5}KAl_{2.5}Si_{5.5}O_{16}·5H_2O$)	-39.9±1.2	-8741.26	-9461.67	707[d]	626[d]	304.74
D4R	LTA ($Na_{1.98}Al_{1.98}Si_{2.02}O_8·5.31H_2O$)	-18.2±0.6	-5203.75	-5701.89	584[e]	513[e]	186.95
	4Å ($Na_2Al_2Si_2O_8·4.5H_2O$)	-20.5±0.6	-5029.88	-5486.36	536[e]	475[e]	187.00
S6R	SOD(OH) ($Na_8Al_6Si_6O_{24}(OH)_2·2H_2O$)	-65.2±2.0	-13221.4	-14120.1	943[f]	895[f]	424.74
	SOD(Cl) ($Na_8Al_6Si_6O_{24}Cl_2$)	-69.4±2.1	-12719.1	-13473.4	848[g]	812[g]	421.53
	CAN(NO_3) ($Na_8Al_6Si_6O_{24}(NO_3)_2·4H_2O$)	-64.8±1.9	-13600.8	-14717.6	1149[h]	1119[h]	435.96
D6R	CHA(Na) ($Na_2Al_2Si_4O_{12}·6H_2O$)	-31.9±1.0	-7117.55	-7808.31	548[c]	578[c]	249.95
	FAU-X ($Na_2Al_2Si_{2.5}O_9·6.2H_2O$)	-21.9±0.7	-5857.79	-6456.94	566[i]	586[i]	195.80
	FAU-Y ($Na_2Al_2Si_4O_{12}·8H_2O$)	-29.5±0.9	-7578.22	-8352.62	734[i]	739[i]	282.94
4=1	NAT ($Na_2Al_2Si_3O_{10}·2H_2O$)	-26.6±0.8	-5305.15	-5707.02	360[j]	359[j]	169.36
5-1	MOR(Na) ($Na_{0.72}Al_{0.72}Si_{5.28}O_{12}·2.71H_2O$)	-22.5±0.7	-5955.95	-6442.40	388[c]	405[c]	210.59

All values shown were obtained in the current study except where indicated [a] Measured by [17]; [b] Measured by [61]; [c] Calculated using additivity method based on the elementary (hydro)oxide components; [d] Calculated by additivity method starting from zeolites with the PHI framework [11]; [e] Calculated starting from the LTA framework [66]; [f] Measured by [67]; [g] Measured by [68]; [h] Calculated starting from the CAN framework[57]; [i] Indicated by [7]; [j] Measured by [65]; log K_{sp} was calculated with respect to the species of AlO_2^-, Ca^{2+}, Na^+, K^+, SiO_2^0, Cl^-, OH^-, NO_3^-, and H_2O. For the additivity method, the thermodynamic data of the elementary (hydro)oxide components (i.e., zeolitic H_2O, NaOH, $Ca(OH)_2$, KOH, $Al(OH)_3$, SiO_2, NaCl, $NaNO_3$, and Na_2CO_3) was summarized in Table A2 and the reference reactions shown in Table A5.

Table 7. Thermodynamic properties of zeolites reported in the literature. Experimental values (e.g., derived from solubility experiments and calorimetric measurement) were marked in bold.

Zeolite	Formula	log K_{sp} (298.15 K)	ΔG_f^0 kJ/mol	ΔH_f^0 kJ/mol	S^0 J/mol K	C_p J/mol K	Ref
Analcime	$Na_2Al_2Si_4O_{12}\cdot 2H_2O$	-33.47	-6177.8	-6616.9	459	425	[7] [a]
	$Na_{1.98}Al_{1.98}Si_{4.02}O_{12}\cdot 2H_2O$	-32.00	-6178.1	**-6616.0**	**462**	**425**	[61]
	$Na_2Al_2Si_4O_{12}\cdot 2H_2O$	-33.23	-6176.4	-6613.4	469	424	[17]
	$Na_2Al_2Si_4O_{12}\cdot 2H_2O$	-34.74	-6192.6	-6624.0			[13]
	$Na_2Al_2Si_4O_{12}\cdot 2H_2O$	**-32.12**	**-6178.4**				[62]
	$Na_2Al_2Si_4O_{12}\cdot 2H_2O$	**-29.30 ± 0.4**	**-6160.2**				[64]
	$Na_2Al_2Si_4O_{12}\cdot 2H_2O$				**468.6 ± 1.2**	**419.8**	[69]
Natrolite	$Na_2Al_2Si_3O_{10}\cdot 2H_2O$	-26.43	-5316.7	**-5718.6**	**360**	**359**	[65]
	$Na_2Al_2Si_3O_{10}\cdot H_2O$				**425**	**380**	[17]
	$Na_2Al_2Si_3O_{10}\cdot 2H_2O$	**-30.20**	**-5325.7**	**-5728.0**	**360**	359	[7]
Gismondine	$CaAl_2Si_2O_8\cdot 4.5H_2O$ [b]	-26.25	-5102.4	-5589.9	371	435	[11]
Zeolite P	$CaAl_2Si_2O_8\cdot 4.5H_2O$ [b]	-23.17	-5084.8	-5564.6	397	459	[11]
	$CaAl_2Si_2O_8\cdot 4.5H_2O$ [b]	**-20.30**	**-5057.8**	**-5424.0**	**779**	753	[7]
Phillipsite	$Na_2Al_2Si_6O_{16}\cdot 6H_2O$	-42.84	-8863.7	-9623.3	**764**	**662**	[11]
	$K_2Al_2Si_6O_{16}\cdot 6H_2O$ [b]	-45.66	-8920.9	-9683.7	**780**	**702**	[11]
	$CaAl_2Si_6O_{16}\cdot 6H_2O$ [b]	-41.10	-8882.7	-9648.0	**684**	**644**	[11]
	$Na_{1.08}K_{0.80}Al_{1.88}Si_{6.12}O_{16}\cdot 6H_2O$ [b]				**771.9 ± 2.4**	**786.2**	[70]
	$CaAl_2Si_6O_{16}\cdot 6H_2O$ [b]				**697**	**586**	[17]
Zeolite A	$Na_2Al_2Si_2O_8$		-3899.2	**-4121.7**	**271**	**260**	[66]
	$Na_2Al_2Si_{2.12}O_{8.24}$	-23.24 [c]	-4078.4				[16]
	$Na_{2.0}Al_{2.0}Si_{2.0}O_{8.0}\cdot 4.36H_2O$			**-5454.8**			[13]
Cancrinite	$Na_{8.28}Al_{5.93}Si_{6.07}O_{24}(CO_3)_{0.93}(OH)_{0.49}\cdot 3.64H_2O$		-13690.0 ± 51	**-14684.0 ± 50**	**1057 ± 35**	**1047 ± 30**	[57]
	$Na_{7.282}Al_{5.854}Si_{6.146}O_{24}(NO_3)_{1.336}(CO_3)_{0.046}\cdot 3.365H_2O$			**-14258.3 ± 17.3**			[60]
Sodalite-Cl	$Na_8Al_6Si_6O_{24}Cl_2$		-12703.7	**-13457.9**	**848**	**812**	[68]
Hydrosodalite	$Na_8Al_6Si_6O_{24}(OH)_2\cdot 2H_2O$		-13384.2	**-14283.0**	**943**	**895**	[67]
	$Na_{7.26}Al_6Si_{6.21}O_{24.03}(OH)_{1.68}\cdot 2.91H_2O$	-60.34 [d]					[71]
Chabazite	$CaAl_2Si_4O_{12}\cdot 6H_2O$ [b]	-34.22	-7173.6	**-7824.4**	**614**	**643**	[11]
	$CaAl_2Si_4O_{12}\cdot 6H_2O$ [b]				**640**	**589**	[61]
	$CaAl_2Si_4O_{12}\cdot 6H_2O$ [b]	**-25.80**	**-7111.8**	**-7774.0**	581 [e]	617 [e]	[7]
Faujasite(X)	$Na_2Al_2Si_{2.5}O_9\cdot 6.2H_2O$	**-20.10**	**-5847.5**	**-6447.0**	**566**	586	[7]
Faujasite(Y)	$Na_2Al_2Si_4O_{12}\cdot 8H_2O$	**-25.00**	**-7552.5**	**-8327.0**	**734**	739	[7]
Mordenite	$Ca_{0.25}K_{0.15}Na_{0.35}AlSi_5O_{12}\cdot 3.667H_2O$		-6294.6	-6807.6			[13]
	$Ca_{0.289}Na_{0.361}Al_{0.940}Si_{5.060}O_{12}\cdot 3.468H_2O$		-6229.89	-6738.44	486.54	484.45	[11]
	$Ca_{0.289}Na_{0.361}Al_{0.940}Si_{5.060}O_{12}\cdot 3.468H_2O$		-6247.6 ± 4.5	**-6756.2 ± 4.5**	**486.54 ± 0.97**	**484.33 ± 0.97**	[72]
	$Ca_{0.29}Na_{0.36}Al_{0.94}Si_{5.06}O_{12}\cdot 3.47H_2O$		-6227.9	-6736.7	486.5		[17]

[a] Derived from [61]; [b] Data of Ca and K endmembers are shown for comparison; [c] Estimated from [73]; [d] log K_{sp} is extrapolated value based on [74, 75]; [e] Recalculated for $CaAl_2Si_4O_{12}\cdot 6H_2O$ from the values measured by [76] for natural chabazite.

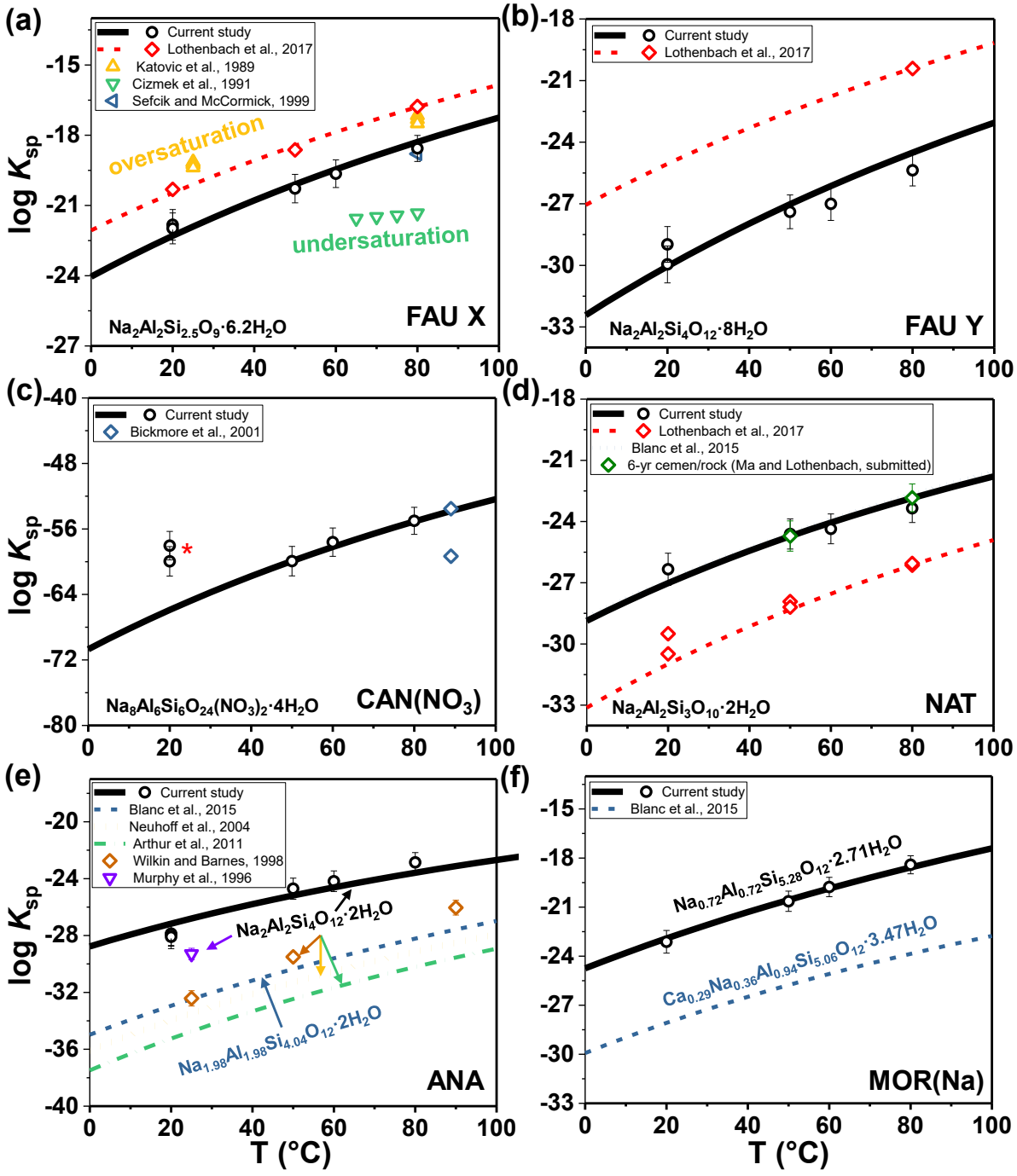

Figure 4. Log solubility products, K_{sp} for (a) FAU-X, (b) FAU-Y, (c) CAN(NO_3), (d) NAT, (e) ANA, and (f) MOR(Na). Values derived from current study are indicated by the black hollow dots and bold lines. For comparison, solubility products and the relevant curves with temperature [7, 11, 13, 22, 54-56, 58, 61, 62, 64, 77] were also plotted. * Data points excluded in the fits.

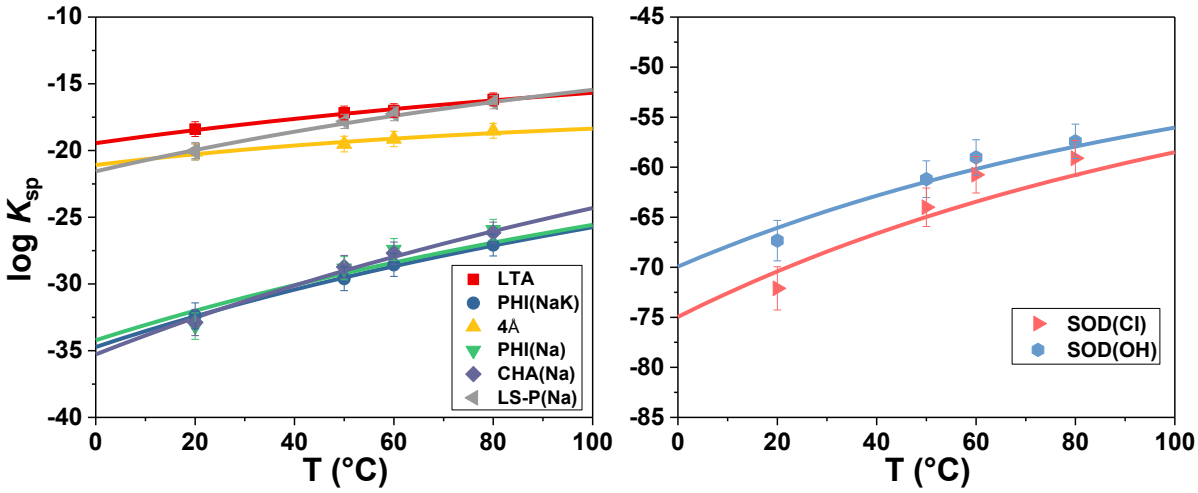

Figure 5. Experimental log K_{sp} values of different zeolites at 20, 50, 60, and 80 °C. The solid lines were generated with the GEMS code using the thermodynamic data and the chemical compositions compiled in Table 6.

3.3. Predominance diagrams in the chemical sub-systems of Na_2O-SiO_2-Al_2O_3-H_2O

As the newly generated thermodynamic data of Na-based zeolites are devised as an addition to the Cemdata database, the consistency between thermodynamic data of zeolites, clays/micas, and SiO_2/$Al(OH)_3$ was examined by establishing their predominance diagrams for the Na_2O-SiO_2-Al_2O_3-H_2O system at 25 and 80°C. The data shown in Figure 6 and 7, exhibit in general a similar sequence of predominance as reported in Blanc et al. [11], indicating a good compatibility of the derived zeolite data with the stability of $Al(OH)_3$ and with clays. However, the stable zeolites predicted show some clear differences, in the present study in addition to natrolite, also Na-chabazite and Na-mordenite were calculated to be stable.

For the $Al(OH)_3$-saturated chemical system, the presence of microcrystalline $Al(OH)_3$ (Figure 6a) and gibbsite (Figure 6b) were considered at 25 °C as $Al(OH)_3$ with poor crystallinity could be thermodynamically favored at room temperature. Compared to the diagrams with gibbsite, microcrystalline $Al(OH)_3$ had as expected a more limited predominance area, while the stability domains of its neighbor phases expanded. In addition of the neighboring minerals, paragonite and kaolinite, two clay minerals, beidellite(Na) and pyrophyllite, were predicted to predominate the corresponding regions in agreement with Blanc et al. [11]. Besides,

the domains characterized by either high [Si] or high alkalinity were predominated by three types of zeolite, i.e., NAT, CHA(Na), and MOR(Na). At 25 °C, the stability domains of zeolites were mainly occupied by CHA(Na) and MOR(Na) under low and high [Si], respectively. With increasing temperature, the stability domains of NAT expanded, resulting in a decrease of the stability region of CHA(Na).

For the SiO_2-saturated chemical system, again the presence of either amorphous SiO_2 or quartz was considered at 25 °C (Figure 7a and 7b). Due to the high solubility of amorphous SiO_2, the stability domain of am-SiO_2 was much smaller than that of quartz. Both quartz and gibbsite showed larger stability domain areas at higher temperature (i.e., 80 °C), indicating that these crystalline phases were more stable thermodynamically at higher temperatures. In the chemical system saturated with amorphous SiO_2, the resulting higher [Si] compared to the case of quartz stabilized the most siliceous zeolite [10], i.e., MOR(Na), at relatively low aluminum concentrations. In addition of the three zeolites observed in the $Al(OH)_3$-saturated system, LS-P(Na) with a very low Si/Al ratio of 1 appeared at the top right part of the diagram, suggesting that LS-P(Na) can be stabilized by high Al and Na concentrations. The Si/Al ratios of MOR(Na), CHA(Na), NAT, and LS-P(Na) are 7.35, 2.00, 1.50, and 1.00, respectively. As can be seen, the four zeolites predominate in sequence as [Al] increases, in good accordance with their Si/Al ratios. For 80°C, a similar predominance diagram was calculated, the main difference is that the stability field of CHA(Na) was clearly smaller.

For the system saturated by quartz at 25 °C, the resulting higher [Si] destabilized MOR(Na) and the CHA(Na) region was also reduced. A significant change of the stability domain of NAT and CHA(Na) with temperature was observed similar to the $Al(OH)_3$-saturated system. CHA(Na) was predicted to be destabilized at 80°C with respect to NAT indicates that NAT is stabilized at higher temperature.

732 The zeolites of the S6R group (sodalites and cancrinite) were not included during the calcula-
733 tion of predominance diagrams as no Cl^- or NO_3^- are present in the cement-zeolite-clay sys-
734 tem. In the investigated chemical system, LTA, FAU, PHI, and ANA were undersaturated
735 compared to NAT, CHA(Na), MOR(Na) and LS-P(Na). As discussed above, LTA and FAU
736 might be the intermediate phases regarding the more stable phases of LS-P(Na) and
737 CHA(Na), respectively. However, analcime was not predicted in the temperature range of 25
738 to 80 °C although it is one of the most common zeolites at the earth's surface. Its composi-
739 tional ratio range is quite small with the number of Si atoms ranging from 1.8 to 2.3 for six
740 oxygen atoms [61]. Analcime was commonly observed to form in the alteration process of
741 clays (e.g., smectite and bentonite) under hyperalkaline (pH>13.5) conditions from 90 °C to
742 200 °C [78]. Higher reaction temperatures and higher Na concentrations promoted the for-
743 mation of analcime. Besides, the stability domain of analcime calculated by Blanc et al. [11]
744 at 25°C was very narrow, indicating that its formation at lower temperature was not favored.
745 In the current work, the absence of analcime in predominance diagrams at 25 and 80°C is due
746 to its relatively higher solubility determined here for synthetic samples compared to the litera-
747 ture values on natural samples; extrapolation of the solubility to higher temperature indicated
748 the stabilization of analcime with respect to FAU-Y and CHA(Na) from 110 °C and from
749 150 °C, respectively (Figure A7).
750 Phillipsite (mostly K-based phillipsite) and chabazite were also commonly observed in ce-
751 ment/clay interaction systems as reported in the review by Gaucher and Blanc [78]. However,
752 Na-phillipsite was missing in the calculated predominance diagrams, where CHA(Na) was
753 predicted to be more stable than PHI(Na), as the Si/Al ratio (2.2) of PHI(Na)
754 ($Na_{2.5}Al_{2.5}Si_{5.5}O_{16}\cdot 4H_2O$) is quite close to that (2.0) of CHA(Na) ($Na_2Al_2Si_4O_{12}\cdot 6H_2O$). It
755 seems quite unlikely that phillipsite could be an intermediate phase. Typically, phillipsite pre-
756 fers to accommodate different types of extraframework cations together, e.g., K^+ plus Na^+

and/or Ca^{2+} [46]. K-prevailing phillipsite with other cations doped is the most common in nature and thus the most stable in thermodynamics. The phillipsite currently investigated is purely Na-based and thus less stable than K-containing phillipsites [11], such that it can be expected that in systems containing Ca, K and Na phillipsite would be stable. In addition, the Si/Al ratio (2.2) of PHI(Na) ($Na_{2.5}Al_{2.5}Si_{5.5}O_{16}\cdot 4H_2O$) was quite close to 2.0, the ratio of CHA(Na) ($Na_2Al_2Si_4O_{12}\cdot 6H_2O$). In the predominance diagrams, CHA(Na) was predicted more stable than PHI(Na) and thus covered up PHI(Na) in stability domain. These could explain the reported frequent occurrence of phillipsite [78] although it is not predicted in a pure Na-system.

In contrast, mordenite is rarely reported in clay/cement experiments except by [78], but predicted here to occur. Mordenite is a high-silica zeolite with Si/Al ratios ranging from 4.0 to 6.1. The Al content available in many clay/cement experiments could be too high to facilitate the formation of mordenite. In the predominance diagrams in the current study all the investigated Na-based zeolites were enabled to precipitate. Therefore, the predominance results only obeyed the extent of oversaturation but might not agree exactly with the natural abundance or previous mineral observations where no such zeolite was formed.

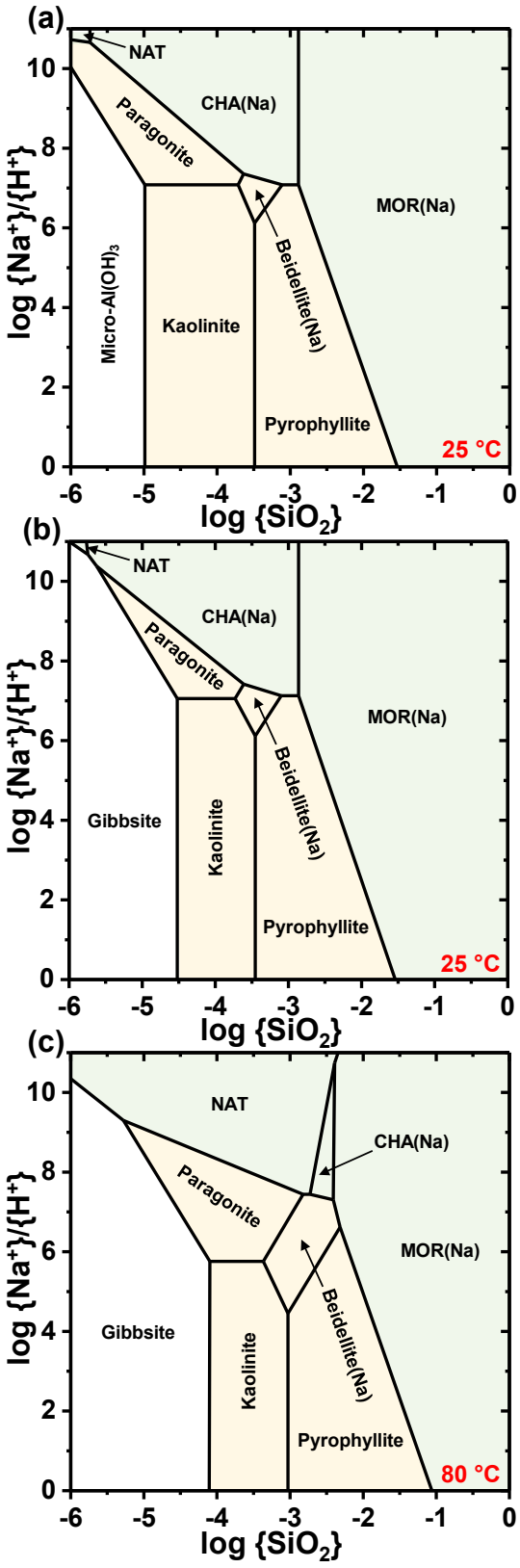

773

774 **Figure 6.** Predominance diagrams in Na_2O-SiO_2-Al_2O_3-H_2O chemical systems for zeolite
775 (light green), clay and mica (light yellow), and $Al(OH)_3$ (colorless) phases. (a) saturated with
776 respect to microcrystalline $Al(OH)_3$ (micro-$Al(OH)_3$) at 25 °C; saturated with respect to
777 gibbsite (b) at 25 °C and (c) at 80 °C.

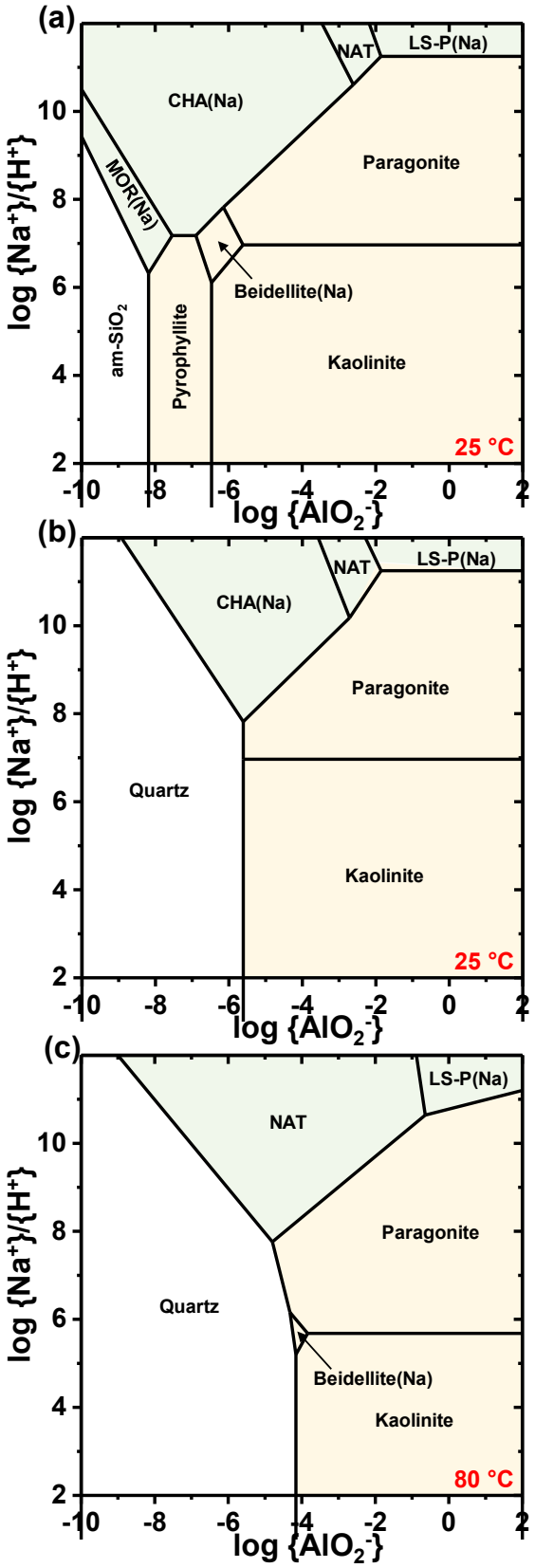

Figure 7. Predominance diagrams in Na_2O-SiO_2-Al_2O_3-H_2O chemical systems for zeolite (light green), clay and mica (light yellow), and SiO_2 (colorless) phases. (a) saturated with respect to amorphous SiO_2 (am-SiO_2) at 25 °C; saturated with respect to quartz (b) at 25 °C and (c) at 80 °C.

4. Conclusions

In this study, Na-based zeolites of six different secondary building units (i.e., S4R, D4R, S6R, D6R, 4=1, and 5-1) were synthesized via hydrothermal methods in a temperature range of 80 to 200 °C. In addition, a typical molecular sieve 4Å (LTA type) was also investigated. The framework structures, the ratios between extra-framework cations, Si, and Al, and the water contents of these different zeolites were determined by XRD, SEM-EDS, and TGA, respectively. The low-frequency bonding vibrations of zeolite structures were characterized by FT-IR, showing that zeolites having the same secondary building units always have similar IR band features. The solid characterization results indicated that the targeted zeolites were synthesized successfully with high purity. The precise element composition and framework structure type (i.e., ANA, GIS, PHI, LTA, SOD, CAN, CHA, FAU, NAT, or MOR) of each zeolite were thus identified.

The solubility of these zeolites was investigated from under-saturation at 20, 50, 60, and 80 °C and compared where possible with literature values. Based on these solubility measurements log K_{sp} and $\Delta_f G^0$ values at different temperatures, could be calculated. Completing these data with measured or calculated data for the heat capacity, C_p^0, and entropy, S^0, data allowed to compute the solubility of the zeolites at 25 °C and its changes with temperature using GEM-Selektor. Differences in log K_{sp} values were observed between the data measured in this paper and the literature values, especially for analcime, in which case the synthetic ANA resulted in roughly 4 log units larger solubility product than previously reported for natural analcime [62] but showed comparable results to another natural analcime [64].

Predominance diagrams in the chemical sub-systems of Na_2O-SiO_2-Al_2O_3-H_2O were established successfully and compared with literature. The derived database for Na-based zeolites is compatible with the Cemdata18 database and the thermodynamic data of the selected Na-based clays and micas in the literature. The experimentally derived thermodynamic data partly

reflect the early stage of the zeolite ageing, which could provide insights on the zeolite formation process not only in the context of radioactive waste disposal but also in environments where zeolites could exist (such as the cementitious material hydration system). In future, further careful data collations and verifications (e.g., the S^0 value derived from limited solubility data points, the larger log K_{sp} value of ANA probably caused by poorer crystallinity, etc.) require further consideration.

This database for Na-containing zeolites is freely downloadable at http://www.empa.ch/cemdata in formats supporting the computer programs GEM-Selektor [32, 79] and in PHREEQC format.

Acknowledgements

We thank the anonymous reviewers for their constructive suggestions and comments. The following funding resources for this research are acknowledged: (a) Distinguished Senior Researcher Grant at Empa, (b) European Union's Horizon 2020 research and innovation programme under the Marie Skłodowska-Curie grant agreement number 754364 and (c) Nagra grant, grant number 16675. Luigi Brunetti is acknowledged for measurements of the ion concentration of the solution, Biwan Xu for SEM-EDS measurements, Yiru Yan for FT-IR acquisitions, Boris Ingold for the lab support, and Frank Winnefeld for help and discussion with XRD measurement and results.

Appendix

Supplementary data to this article can be found online.

References

[1] J. Čejka, H. van Bekkum, A. Corma, F. Schüth, Introduction to Zeolite Science and Practice, third ed., Elsevier, Oxford, U.K., 2007.

[2] B. Ahmadi, M. Shekarchi, Use of natural zeolite as a supplementary cementitious material, Cem. Concr. Compos. 32 (2010) 134-141.

[3] C. Shi, A. Fernández-Jiménez, Stabilization/solidification of hazardous and radioactive wastes with alkali-activated cements, J. Hazard. Mater. 137 (2006) 1656-1663.

[4] J.L. Provis, G.C. Lukey, J.S.J. van Deventer, Do geopolymers actually contain nanocrystalline zeolites? A reexamination of existing results, Chem. Mater. 17 (2005) 3075-3085.

[5] M.D. Jackson, S.R. Mulcahy, H. Chen, Y. Li, Q. Li, P. Cappelletti, H.-R. Wenk, Phillipsite and Al-tobermorite mineral cements produced through low-temperature water-rock reactions in Roman marine concrete, Am. Mineral. 102 (2017) 1435-1450.

[6] Z. Shi, C. Shi, J. Zhang, S. Wan, Z. Zhang, Z. Ou, Alkali-silica reaction in waterglass-activated slag mortars incorporating fly ash and metakaolin, Cem. Concr. Res. 108 (2018) 10-19.

[7] B. Lothenbach, E. Bernard, U. Mäder, Zeolite formation in the presence of cement hydrates and albite, Phys. Chem. Earth. Parts A/B/C 99 (2017) 77-94.

[8] R. Fernández, M. Rodríguez, R.V.d.l. Villa, J. Cuevas, Geochemical constraints on the stability of zeolites and C–S–H in the high pH reaction of bentonite, Geochim. Cosmochim. Acta 74 (2010) 890-906.

[9] S. Choi, G. Crosson, K.T. Mueller, S. Seraphin, J. Chorover, Clay mineral weathering and contaminant dynamics in a caustic aqueous system: II. Mineral transformation and microscale partitioning, Geochim. Cosmochim. Acta 69 (2005) 4437-4451.

859 [10] D. Savage, C. Walker, R. Arthur, C. Rochelle, C. Oda, H. Takase, Alteration of bentonite
860 by hyperalkaline fluids: A review of the role of secondary minerals, Phys. Chem. Earth. Parts
861 A/B/C 32 (2007) 287-297.
862 [11] P. Blanc, P. Vieillard, H. Gailhanou, S. Gaboreau, N. Marty, F. Claret, B. Madé, E.
863 Giffaut, ThermoChimie database developments in the framework of cement/clay interactions,
864 Appl. Geochem. 55 (2015) 95-107.
865 [12] S.J. Chipera, J.A. Apps, Geochemical stability of natural zeolites, Rev. Mineral.
866 Geochem. 45 (2001) 117-161.
867 [13] R. Arthur, H. Sasamoto, C. Walker, M. Yui, Polymer model of zeolite thermochemical
868 stability, Clays Clay Miner. 59 (2011) 626-639.
869 [14] S.V. Mattigod, B.P. McGrail, Estimating the standard free energy of formation of
870 zeolites using the polymer model, Microporous Mesoporous Mater. 27 (1999) 41-47.
871 [15] J.A. Chermak, J.D. Rimstidt, Estimating the thermodynamic properties (ΔG_f^0 and ΔH_f^0)
872 of silicate minerals at 298 K from the sum of polyhedral contributions, Am. Mineral. 74
873 (1989) 1023-1031.
874 [16] A. La Iglesia, A.J. Aznar, A method of estimating the Gibbs energies of formation of
875 zeolites, Zeolites 6 (1986) 26-29.
876 [17] H.C. Helgeson, J.M. Delany, H.W. Nesbitt, D.K. Bird, Summary and critique of the
877 thermodynamic properties of rock-forming minerals, Am. J. Sci. 278 (1978) 1-229.
878 [18] R.J. Myers, B. Lothenbach, S.A. Bernal, J.L. Provis, Thermodynamic modelling of
879 alkali-activated slag cements, Appl. Geochem. 61 (2015) 233-247.
880 [19] G.M. Anderson, D.A. Crerar, Thermodynamics in Geochemistry: The Equilibrium
881 Model, Oxford University Press, 1993.
882 [20] B. Lothenbach, D.A. Kulik, T. Matschei, M. Balonis, L. Baquerizo, B. Dilnesa, G.D.
883 Miron, R.J. Myers, Cemdata18: A chemical thermodynamic database for hydrated Portland
884 cements and alkali-activated materials, Cem. Concr. Res. 115 (2019) 472-506.

885 [21] E. Giffaut, M. Grivé, P. Blanc, P. Vieillard, E. Colàs, H. Gailhanou, S. Gaboreau, N.
886 Marty, B. Madé, L. Duro, Andra thermodynamic database for performance assessment:
887 ThermoChimie, Appl. Geochem. 49 (2014) 225-236.
888 [22] B. Ma, B. Lothenbach, Thermodynamic study of cement/rock interactions using
889 experimentally generated solubility data of zeolites (Under revision).
890 [23] J. Shin, N.H. Ahn, M.A. Camblor, C.M. Zicovich-Wilson, S.B. Hong, Synthesis of
891 aluminosilicate natrolites and control of their tetrahedral atom ordering, Chem. Mater. 26
892 (2014) 3361-3363.
893 [24] B.R. Albert, A.K. Cheetham, C.J. Adams, Investigations on P zeolites: Synthesis and
894 structure of the gismondine analogue, highly crystalline low-silica CaP, Microporous
895 Mesoporous Mater. 21 (1998) 127-132.
896 [25] B.R. Albert, A.K. Cheetham, J.A. Stuart, C.J. Adams, Investigations on P zeolites:
897 Synthesis, characterisation, and structure of highly crystalline low-silica NaP, Microporous
898 Mesoporous Mater. 21 (1998) 133-142.
899 [26] S.N. Azizi, A. Alavi Daghigh, M. Abrishamkar, Phase transformation of zeolite P to Y
900 and analcime zeolites due to changing the time and temperature, J. Spectro. 2013 (2013) 1-5.
901 [27] D.E. Akporiaye, I.M. Dahl, H.B. Mostad, R. Wendelbo, Aluminum distribution in
902 chabazite: An experimental and computational study, J. Phys. Chem. 100 (1996) 4148-4153.
903 [28] R.K. Singh, P. Webley, Adsorption of N_2, O_2, and Ar in potassium chabazite, Adsorption
904 11 (2005) 173-177.
905 [29] S. Mintova, Verified Synthesis of Zeolitic Materials, third ed., Gulf Professional
906 Publishing, Elsevier, 2016.
907 [30] J. Yuan, J. Yang, H. Ma, C. Liu, C. Zhao, Hydrothermal synthesis of analcime and
908 hydroxycancrinite from K-feldspar in Na_2SiO_3 solution: Characterization and reaction
909 mechanism, RSC Adv. 6 (2016) 54503-54509.

910 [31] L. Wu, A. Navrotsky, Synthesis and thermodynamic study of transition metal ion (Mn^{2+},
911 Co^{2+}, Cu^{2+}, and Zn^{2+}) exchanged zeolites A and Y, Phys. Chem. Chem. Phys. 18 (2016)
912 10116-10122.
913 [32] D.A. Kulik, T. Wagner, S.V. Dmytrieva, G. Kosakowski, F.F. Hingerl, K.V. Chudnenko,
914 U.R. Berner, GEM-Selektor geochemical modeling package: revised algorithm and GEMS3K
915 numerical kernel for coupled simulation codes, Comput. Geosci. 17 (2013) 1-24.
916 [33] T. Thoenen, W. Hummel, U. Berner, E. Curti, The PSI/Nagra chemical thermodynamic
917 database 12/07, Nagra Working Report NAB, 2014.
918 [34] R.J. Myers, S.A. Bernal, J.L. Provis, A thermodynamic model for C-(N-)ASH gel:
919 CNASH_ss. Derivation and validation, Cem. Concr. Res. 66 (2014) 27-47.
920 [35] D.L. Parkhurst, C. Appelo, Description of input and examples for PHREEQC version 3:
921 A computer program for speciation, batch-reaction, one-dimensional transport, and inverse
922 geochemical calculations, US Geological Survey, 2013.
923 [36] D. Kinniburgh, D. Cooper, PhreePlot: Creating graphical output with PHREEQC, 2011.
924 [37] E. Giffaut, M. Grivé, P. Blanc, P. Vieillard, E. Colàs, H. Gailhanou, S. Gaboreau, N.
925 Marty, B. Made, L. Duro, Andra thermodynamic database for performance assessment:
926 ThermoChimie, Appl. Geochem. 49 (2014) 225-236.
927 [38] B.J. Merkel, B. Planer-Friedrich, Groundwater Geochemistry: A Practical Guide to
928 Modeling of Natural and Contaminated Aquatic Systems, Springer, Berlin, 2008.
929 [39] J. Setschenow, Über die konstitution der salzlösungen auf grund ihres verhaltens zu
930 kohlensäure, Zeitschrift für Physikalische Chemie 4 (1889) 117-125.
931 [40] R.G. Berman, Internally-consistent thermodynamic data for minerals in the system
932 Na_2O-K_2O-CaO-MgO-FeO-Fe_2O_3-Al_2O_3-SiO_2-TiO_2-H_2O-CO_2, J. Petrol. 29 (1988) 445-522.
933 [41] D.A. Kulik, Minimising Uncertainty Induced by Temperature Extrapolations of
934 Thermodynamic Data: A Pragmatic View on the Integration of Thermodynamic Databases
935 into Geochemical Computer Codes, Nuclear Energy Agency of the OECD (NEA), 2002.

936 [42] R.A. Robie, B.S. Hemingway, Thermodynamic Properties of Minerals and Related
937 Substances at 298.15 K and 1 bar (10^5 Pascals) Pressure and at Higher Temperatures (Vol.
938 2131), US Government Printing Office, Washington, U.S., 1995.
939 [43] M.W.J. Chase, NIST-JANAF Thermochemical Tables: National Institute of Standards
940 and Technology (fourth edition), J Phys Chem Ref Data, 9 (1998).
941 [44] T. Frising, P. Leflaive, Extraframework cation distributions in X and Y faujasite zeolites:
942 A review, Microporous Mesoporous Mater. 114 (2008) 27-63.
943 [45] G. Vezzalini, S. Quartieri, A. Alberti, Structural modifications induced by dehydration in
944 the zeolite gismondine, Zeolites 13 (1993) 34-42.
945 [46] G. Glauco, G. Ermanno, Natural Zeolites, Springer, 1985.
946 [47] K.F. Fischer, V. Schramm, Crystal structure of gismondite, a detailed refinement, in:
947 E.M. Flanigen, L.B. Sand (Eds.), Molecular Sieve Zeolites-I, Advances in Chemistry,
948 American Chemical Society, 1974, pp. 250-258.
949 [48] R. Barrer, J. Cole, H. Villiger, Chemistry of soil minerals. Part VII. Synthesis, properties,
950 and crystal structures of salt-filled cancrinites, J. Chem. Soc. A (1970) 1523-1531.
951 [49] E.M. Flanigen, H. Khatami, H.A. Szymanski, Infrared Structural Studies of Zeolite
952 Frameworks, in: E.M. Flanigen, L.B. Sand (Eds.), Molecular Sieve Zeolites-I, Advances in
953 Chemistry, American Chemical Society, 1974, pp. 201-229.
954 [50] W. Mozgawa, M. Krol, K. Barczyk, FT-IR studies of zeolites from different structural
955 groups, Chemik 65 (2011) 667-674.
956 [51] J. Scherzer, J.L. Bass, Infrared spectra of ultrastable zeolites derived from type Y
957 zeolites, J. Catal. 28 (1973) 101-115.
958 [52] P.D. Glynn, E.J. Reardon, Solid-solution aqueous-solution equilibria; thermodynamic
959 theory and representation, Am. J. Sci. 290 (1990) 164-201.

960 [53] S.M. Leisinger, B. Lothenbach, G. Le Saout, C.A. Johnson, Thermodynamic modeling of
961 solid solutions between monosulfate and monochromate $3CaO \cdot Al_2O_3 \cdot Ca[(CrO_4)_x(SO_4)_{1-x}] \cdot nH_2O$, Cem. Concr. Res. 42 (2012) 158-165.
963 [54] J. Šefčík, A.V. McCormick, Prediction of crystallization diagrams for synthesis of
964 zeolites, Chem. Eng. Sci. 54 (1999) 3513-3519.
965 [55] A. Čizmek, L. Komunjer, B. Subotić, M. Široki, S. Rončević, Kinetics of zeolite
966 dissolution. Part 2. Dissolution of zeolite X in hot sodium hydroxide solutions, Zeolites 11
967 (1991) 810-815.
968 [56] A. Katović, B. Subotić, I. Šmit, L.A. Despotović, M. Ćurić, Role of gel aging in zeolite
969 crystallization, in: M.L. Occelli, H.E. Robson (Eds.), Zeolite Synthesis, ACS Symposium
970 Series, American Chemical Society, 1989, pp. 124-139.
971 [57] S.V. Kurdakova, R.O. Grishchenko, A.I. Druzhinina, L.P. Ogorodova, Thermodynamic
972 properties of synthetic calcium-free carbonate cancrinite, Phys. Chem. Miner. 41 (2014) 75-
973 83.
974 [58] B.R. Bickmore, K.L. Nagy, J.S. Young, J.W. Drexler, Nitrate-cancrinite precipitation on
975 quartz sand in simulated hanford tank solutions, Environ. Sci. Technol. 35 (2001) 4481-4486.
976 [59] E.C. Moloy, Q. Liu, A. Navrotsky, Formation and hydration enthalpies of the
977 hydrosodalite family of materials, Microporous Mesoporous Mater. 88 (2006) 283-292.
978 [60] Q. Liu, H. Xu, A. Navrotsky, Nitrate cancrinite: Synthesis, characterization, and
979 determination of the enthalpy of formation, Microporous Mesoporous Mater. 87 (2005) 146-
980 152.
981 [61] P.S. Neuhoff, G.L. Hovis, G. Balassone, J.F. Stebbins, Thermodynamic properties of
982 analcime solid solutions, Am. J. Sci. 304 (2004) 21-66.
983 [62] R.T. Wilkin, H.L. Barnes, Solubility and stability of zeolites in aqueous solution; I,
984 Analcime, Na-, and K-clinoptilolite, Am. Mineral. 83 (1998) 746-761.

985 [63] L.G. Benning, R.T. Wilkin, H.L. Barnes, Solubility and stability of zeolites in aqueous
986 solution: II. Calcic clinoptilolite and mordenite, Am. Mineral. 85 (2000) 495-508.
987 [64] W.M. Murphy, R.T. Pabalan, J.D. Prikryl, C.J. Goulet, Reaction kinetics and
988 thermodynamics of aqueous dissolution and growth of analcime and Na-clinoptilolite at
989 25 °C, Am. J. Sci. 296 (1996) 128-186.
990 [65] G. Johnson, H. Flotow, P. O'Hare, W. Wise, Thermodynamic studies of zeolites;
991 natrolite, mesolite and scolecite, Am. Mineral. 68 (1983) 1134-1145.
992 [66] L. Qiu, V. Murashov, M.A. White, Zeolite 4A: heat capacity and thermodynamic
993 properties, Solid State Sci. 2 (2000) 841-846.
994 [67] H. Park, P. Englezos, Thermodynamic modeling of sodium aluminosilicate formation in
995 aqueous alkaline solutions, Ind. Eng. Chem. Res. 38 (1999) 4959-4965.
996 [68] N. Komada, J.E.F. Westrum, B.S. Hemingway, M.Y. Zolotov, Y.V. Semenov, I.L.
997 Khodakovsky, L.M. Anovitz, Thermodynamic properties of sodalite at temperatures from 15
998 K to 1000 K, J. Chem. Thermodyn. 27 (1995) 1119-1132.
999 [69] E.G. King, Low temperature heat capacity and entropy at 298.16 K of analcite, J. Am.
1000 Chem. Soc. 77 (1955) 2192-2193.
1001 [70] B.S. Hemingway, R.A. Robie, Thermodynamic properties of zeolites: low-temperature
1002 heat capacities and thermodynamic functions for phillipsite and clinoptilolite. Estimates of the
1003 thermochemical properties of zeolitic water at low temperature, Am. Mineral. 69 (1984) 692-
1004 700.
1005 [71] Y. Xiong, Solubility constants of hydroxyl sodalite at elevated temperatures evaluated
1006 from hydrothermal experiments: Applications to nuclear waste isolation, Appl. Geochem. 74
1007 (2016) 138-143.
1008 [72] G. Johnson, I. Tasker, H. Flotow, P. O'Hare, W. Wise, Thermodynamic studies of
1009 mordenite, dehydrated mordenite, and gibbsite, Am. Mineral. 77 (1992) 85-93.

[73] P. Vieillard, A predictive model for the entropies and heat capacities of zeolites, Eur. J. Mineral. 22 (2010) 823-836.

[74] D. Palmer, P. Benezeth, D. Wesolowski, S. Hilic, Experimental study of the dissolution of aluminum phases as a function of temperature, caustic concentration and additives, in: P. Crepeau (Eds.), Light Metals, The Minerals, Metals & Materials Society (TMS), 2003, pp. 5-10.

[75] L. Zeng, Z. Li, Solubility and modeling of sodium aluminosilicate in NaOH–$NaAl(OH)_4$ solutions and its application to desilication, Ind. Eng. Chem. Res. 51 (2012) 15193-15206.

[76] I. Belitsky, S. Gabuda, V. Drebushchak, V. Naumov, V. Nogteva, I. Paukov, Heat capacity of chabazite in the temperature-range of 5 to 316 K, entropy and enthalpy at standard conditions, Geokhimiya 3 (1982) 444-446.

[77] M. Atkins, F. Glasser, I. Moron, J. Jack, Thermodynamic modelling of blended cements at elevated temperature (50-90 °C). DOE Report: DoE/HIMP/RR/94.011., 1993.

[78] E.C. Gaucher, P. Blanc, Cement/clay interactions – A review: Experiments, natural analogues, and modeling, Waste Manage. 26 (2006) 776-788.

[79] T. Wagner, D.A. Kulik, F.F. Hingerl, S.V. Dmytrieva, GEM-Selektor geochemical modeling package: TSolMod library and data interface for multicomponent phase models, Can. Mineral. 50 (2012) 1173-1195.